Radio-Frequency Non-Thermal Plasma for CO_2 Dissociation and NO_X Formation for Ammonia Synthesis

Catrin Hannah Jarrett

Master of Science by Research

University of York

Physics, Engineering and Technology

December, 2025

Abstract

Non-thermal plasma provides a pathway to drive dissociation and synthesis reactions at room temperature and atmospheric pressure, offering a potential for more sustainable and diverse production. Two applications explored in this work are CO_2 conversion to CO and nitrogen oxide formation as a preliminary step towards ammonia synthesis, both investigated in an argon-based radio-frequency (RF) capacitively coupled plasma (CCP). This thesis investigates the effects of the variation in generator power, gas composition and total flow rate, and evaluates their influence on the relevant dissociation pathways of CO_2 dissociation and nitrogen oxide formation. Analysis is conducted using Fourier-transform infrared (FTIR) spectroscopy, with product concentrations calculated from absorption spectra. Findings include that lower flow rates show an increase in the production of CO density and yield, but a trade off with energy efficiency. The maximum NO_X density and yield were observed at an O_2/N_2 ratio of approximately 8:4, indicating that this composition provides the most favourable conditions for NO_X formation. Ultimately, the primary objective of this thesis is to support more effective design and operation of radio-frequency driven low-temperature plasma systems. This will be accomplished through the controlled variation of experimental parameters to analyse their impact on dissociation and formation mechanisms. This thesis provides actionable insights for both experimental practice and analytical interpretation for targeted goals.

Acknowledgments

I would like to express my gratitude to Prof Erik Wagenaars; without him, this would not have been achievable to me. From giving me a place to start to providing guidance throughout.

Furthermore, I would like express my appreciation to Kari Niemei (research officer), for helping with setup, laboratory training and any questions I had along the process.

I can not thank them both enough, their time and support have been the most valuable resources for me throughout this process and I am deeply grateful.

Declaration of Authorship

I declare that this thesis is a presentation of original work and I am the sole author. This work has not previously been presented for an award at this, or any other, University. All sources are acknowledged as references.

Contents

List of Figures

1

Introduction

Addressing the challenges of ensuring environmentally sustainable and safe industrial carbon monoxide (CO) and ammonia (NH_3) production calls for innovative approaches. Non-thermal plasma (NTP) emerges as a promising technology to address the problems, due to its energy efficiency and ability to operate at room temperature [1], [2]. This thesis investigates two approaches to using NTP for environmentally sustainable production: converting CO_2 to CO as a waste-removal strategy, and modifying synthesis processes so the processes can be carried out at ambient conditions, focusing on NH_3 production.

The first section of the experiment demonstrates the use of NTP properties to convert a waste reactant to a useful product, in this project specifically CO_2 dissociation into CO. The section investigates how changing experimental parameters affects the process of dissociating CO_2 into CO. The production of CO is useful as it is a valuable component for chemical synthesis, metallurgical applications, the food industry (modified atmosphere packaging) and therapeutic processes [3], [4]. Furthermore, the use of waste CO_2 to create valuable products such as CO offers a way to reduce atmospheric CO_2 and combat global warming, advancing the circular carbon economy [5].

Secondly, the properties of NTP can be used to complement and enhance

well-established chemical processes. This thesis explores the application of NTP in NH_3 synthesis. The NTP has the ability to break the highly stable triple nitrogen bond ($N \equiv N$) at room temperature and atmospheric pressure [6], [7], creating nitrogen oxides that can subsequently react with hydrogen for the production of ammonia. Currently, the process to create ammonia, the Haber-Bosch process (using an iron catalyst to break the N_2 bond), is extremely energy intensive. The process alone annually emits 300 million tons of carbon dioxide and consumes nearly 2% of the world's total energy production [8]. Theoretically, the energy consumption of nitrogen fixation by low temperature plasma compared to standard ammonia synthesis should be lower, creating a path for sustainable production [8].

Beyond the possibility of environmentally sustainable production, the ability of NTP to operate at atmospheric pressure and room temperature would allow these processes to be conducted on a local scale, producing localised sources of carbon monoxide and nitrogen oxides. The process of making nitrogen oxides shows a great number of benefits through decentralisation. Since the 1910s, ammonia has played a crucial role in agriculture and the chemical industry, and it plays a key role in global food security. Decentralising systems would allow for the self-production of fertiliser and fuels on a small scale [8]. In resource-limited areas, integrating renewable energy at a small scale offers a potential pathway for further emission reductions, since decentralised systems operate at smaller production capacities that are more compatible with local renewable energy supply. This approach could improve energy security and food scarcity, especially for remote and resource-limited regions [9], [10], [11]. Another positive effect of the decentralisation of production of CO and NO_X would be the reduction of risk, due to the removal of the need to transport hazardous products such as CO and ammonia [11], [12], [13].

Non-thermal plasma is a specific plasma state where it is in non-equilibrium conditions, with the types of particles (ions, electrons and neutrals) in the plasma having varying translational energy. Non-thermal plasmas

are generated by supplying sufficient energy to accelerate the lighter, more mobile particles in the plasma, i.e., electrons. Due to the inertia of the heavier ions, they are unable to reach the same energy levels. Consequently, electrons can achieve much higher energies, while the other particles remain relatively cool [2], [14]. This is useful for the project as the high energy electrons are now able to interact and initiate reactions through collisions without having to heat the entirety of the plasma. Therefore, processes such as the dissociation of CO_2 to CO and the breaking of the triple bond in nitrogen can occur under milder conditions [15], [16].

The project focuses on generating radio-frequency (RF) capacitively coupled plasmas (CCPs) at atmospheric pressure and room temperature ($\approx$300 K). Driven by a single frequency sinusoidal voltage applied across two parallel electrodes, producing an electric field to accelerate the particles. The driving frequency of the AC field used was 40.68 MHz. Specific frequencies are approved for industrial and scientific use and choosing the third harmonic and not the standard 13.56 MHz is due to it having a positive effect on the dissociation of molecules as it allows for greater stability, coupling efficiency and improved plasma robustness [17], [18]. The reactants are mixed with argon before passing through to lower the breakdown voltage, in accordance with Paschen's Law, which calculates the theoretical breakdown voltage based on the distance between the electrodes. This results in increased dissociation due to an increase in electric discharge producing particles to enhance the dissociation of CO_2, N_2 and O_2 [19], [20], [21].

The initial focus of the research is the dissociation from CO_2 to CO production. Current methods of CO production include the gasification of coal, steam reforming of natural gas and partial oxidation of hydrocarbons. These approaches require a large scale infrastructure, high pressures and high temperatures making them unsuitable for certain sites [22]. Another limitation is that they generate a significant amount of pollutants, and operations are often constrained by regional environmen-

tal regulations. Finally, another constraint is the logistical challenge associated with transporting coal or natural gas, which typically requires the development of substantial infrastructure [23].However, CO production is essential for multiple disciplinary fields including environmental and industrial applications. For example, in the metallurgical industry, CO serves as a critical reducing agent in metal extraction and refining processes [3].

Research has been conducted into the utilisation of low-temperature plasma for the conversion of CO_2 to CO. The systems most commonly explored are dielectric barrier discharges (DBDs) [24], [25], [26], gliding arc (GA) discharges [24], [27], microwave (MW) plasmas [24], [28], [29], [30] and nanosecond pulsed discharges [31]. Microwave plasma studies have achieved the highest energy efficiencies, reaching up to 90%. The conditions for this study were highly specific using supersonic gas flows and reduced pressures (0.132 - 0.263 atm) and were reported in 1980s [29]. However, these efficiencies have not been reproduced, recent studies report values of around 51% [28], [30]. Typically at very high efficiencies (90%) this has the trade off of a low conversion ($\approx 2\%$), which is impractical for industrial use [28]. When using scalable and practical conditions using a standard flow rate and at atmospheric pressure, the efficiency drops to values around 20% with conversion at 30% [28]. The GA discharges demonstrate an attractive balance between energy efficiency and conversion, achieving energy efficiency of up to 43% with a conversion rate of 18% [27], [32]. DBDs have scalable qualities due to their simple design and ability to run at atmospheric pressure [26]. Studies have demonstrated conversion rates of 35% with a 2% energy efficiency. However, energy efficiencies of 5–8% have been achieved, although with the trade-off of lower conversion rates [25]. The previous findings are relevant to the project to contextualise where the research fits into the current landscape. Also, it demonstrates the importance of balancing factors such as energy efficiency, conversion, scalability and operating conditions. Radio-frequency driven CCP in particular offers a mix of promising conversion rates under realistic conditions.

The project then explores the formation of NO_X from a mixture of N_2 and O_2 in argon. Low temperature plasma methods are employed to break the triple nitrogen bond as a preliminary step toward the synthesis of nitrogen and hydrogen. The typical route of ammonia synthesis is the Haber-Bosch process. The Haber-Bosch process uses conditions of extremely high temperatures (400–600 °C), pressures of (100-200 bar) and an additional iron catalyst to overcome the highly stable triple bond of nitrogen ($N \equiv N$) [33], [34], [35]. Due to the harsh conditions of the process there is a demand for substantial energy input. Furthermore, the process has to be performed on a large-scale with continuous operation to be economically viable. Studies with DBD plasmas (with the inclusion of catalysts) conducted at 212.5 °C and at ambient pressure have shown an improvement compared to traditional methods of ammonia synthesis [35]. Currently, low temperature plasma assisted ammonia synthesis has not been scaled up to an industrial scale. Even so its ability to operate at small scales and respond to intermittent energy sources makes it an attractive option for decentralised ammonia production [15].

NO_X formation using low temperature plasma techniques has been studied primarily through gliding arc discharge (GA) [36] and dielectric barrier discharge (DBD) [37]. Gliding arc discharge can achieve the conversion rate of 1.5% [36]. Dielectric barrier discharge has previous advantages as previously stated but studies have provided a conversion rate of only 0.5% [37].

I. Dissociation Pathways

i. CO_2 Dissociation Mechanisms

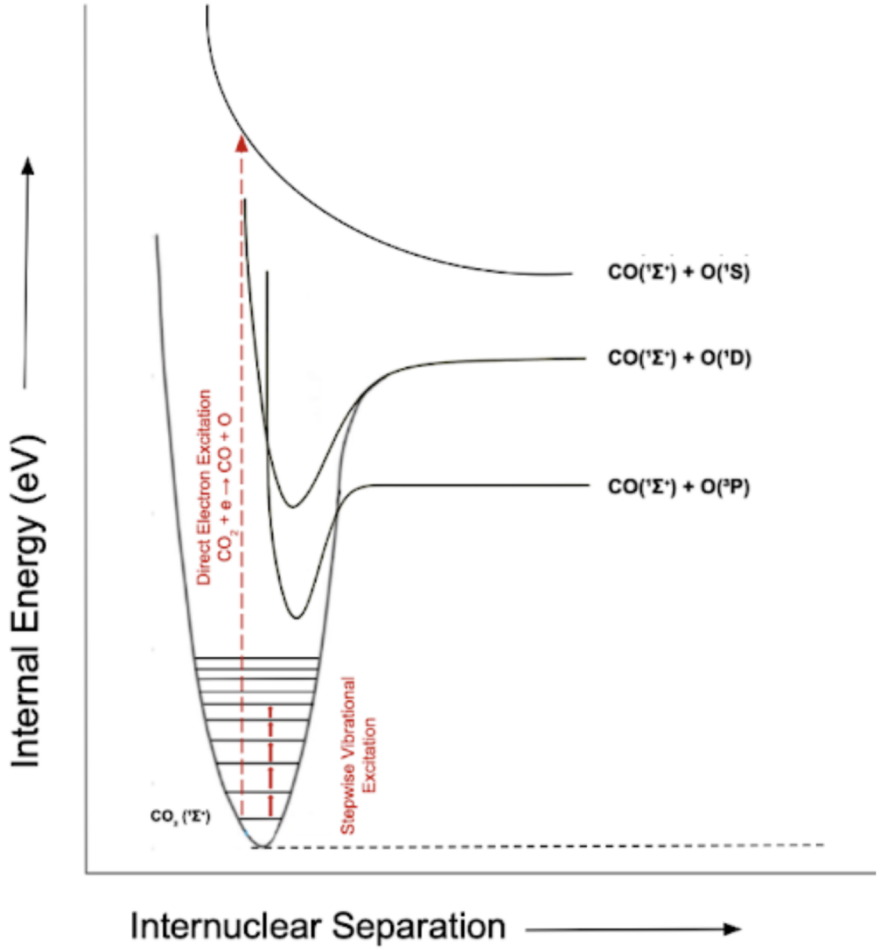

Figure 1.1: Schematic energy diagram of CO_2 dissociation through direct electron excitation and stepwise vibrational excitation. The pathways shown are: $CO(^1\Sigma^+) + O(^3P)$ → ground-state products (∼5.5 eV); $CO(^1\Sigma^+) + O(^1D)$ → excited oxygen (∼7.5 eV); and $CO(^1\Sigma^+) + O(^1S)$ → higher-energy excited oxygen (∼10 eV). Adapted from [38].

CO_2 to CO conversion mechanisms relevant to low temperature plasmas include direct electron impact dissociation and vibrational dissociation. Both of these pathways begin with the dissociation of CO_2, which requires a minimum dissociation energy of 5.5 eV molecule^{-1}.

Thermal dissociation is excluded from this study as the process needs temperatures of above 2000 K to occur, which is avoided with the experimental set-up [39]. Using low temperature plasma allows for energy to not be lost on heating all of the gas when it is only relevant to heat the electrons.

The first relevant pathway is through one-step dissociation via electron impact. This process consists of a high-energy electron exciting the CO_2 molecule from its ground electronic state to a higher electronic state. The molecule subsequently dissociates into a ground electronic CO and an electronically excited oxygen. This process is energy-intensive, requiring an electron energy of at least 7 eV [40].

$$CO_2 + e^- \longrightarrow CO(^1\Sigma^+) + O(^1D) + e^-$$

An indirect dissociation route is vibrational dissociation. In this mechanism, low energy electrons transfer energy to CO_2, exciting the molecule into low-lying energy vibrational states within the electronic ground state [40]. Through subsequent vibrational-vibrational energy exchange, the molecules can "ladder climb" into highly vibrational states. If enough vibrational quanta accumulate to reach roughly 5.5 eV it allows for dissociation to occur. Once this threshold is reached, dissociation can proceed through two possible pathways, both enabled by the accumulated vibrational energy

In low-temperature plasmas, the mean electron temperature is typically in the range of 1–3 eV, which is below the threshold energy for direct electron-impact dissociation of CO_2 ($\tilde{7}$ eV). However, because electron energies are distributed over a range of values rather than being concentrated at the mean, the non-equilibrium electron energy distribution function (EEDF) contains a small population of electrons in a high-energy tail. These electrons can still contribute to direct electron-impact dissociation of CO_2, although with limited efficiency. As a result, direct dissociation is generally not the dominant pathway under these conditions. Instead, stepwise vibrational excitation processes, where electrons

progressively populate vibrational levels of CO_2 before dissociation, can become more important depending on plasma conditions and the shape of the EEDF.

ii. NO_x Formation Mechanisms

The production of NO_X from a mixture of N_2 and O_2 requires the dissociation of molecular nitrogen (N_2) into atomic nitrogen (2N). In low temperature atmospheric plasmas this process can proceed via the main pathways: direct electron impact and vibrational dissociation. However, N_2 presents a challenge for dissociation as it has a strong stable triple bond, which requires a dissociation energy of 9.8 eV. Therefore, making electron impact inefficient as this exceeds the mean electron energy (1-3 eV) in the low temperature plasma [41].

$$N_2 + e^- \longrightarrow 2\,N + e^-$$

Vibrational dissociation is effective at overcoming this barrier. The accumulation of vibrational quanta from molecules leads to a high enough energy for dissociation. This is an effective method due to N_2 having large vibrational level spacing ($\sim$0.3 eV), which is more efficient for preserving vibrational energy due to slower vibrational translation relaxation [41].

The dissociation of O_2 is also a critical step in NO_X formation. Unlike N_2, O_2 has a lower bond dissociation energy of 5.1 eV [42], making direct electron impact dissociation more feasible in low-temperature plasma environments. Vibrational excitation is a contributing pathway to the dissociation of O_2 through the accumulation of energy from surrounding molecules [43].

$$O_2 + e^- \longrightarrow 2\,O + e^-$$

These processes for both N_2 and O_2 can lead to the formation of nitrogen oxides. The dissociated products can undergo oxidation reactions for the

formation of NO_X compounds such as NO and NO_2.

II. Aims of Research

This thesis aims to solidify and advance the understanding of non-thermal plasma possibilities for CO_2 utilisation and nitrogen fixation on a small scale. Through exploring how varying levels of reactant admixture percentage, total flow rate, generator power and N_2 to O_2 ratio affects the product density, yield and energy efficiency in low temperature plasma systems. By varying these parameters it allows insight into how to optimise processes, validate experimental consistency (direct comparison with previous MSc student's results) and evaluate the balance between conversion, energy efficiency, practicality and purpose.

2

Methodology

I. Experimental Set-Up

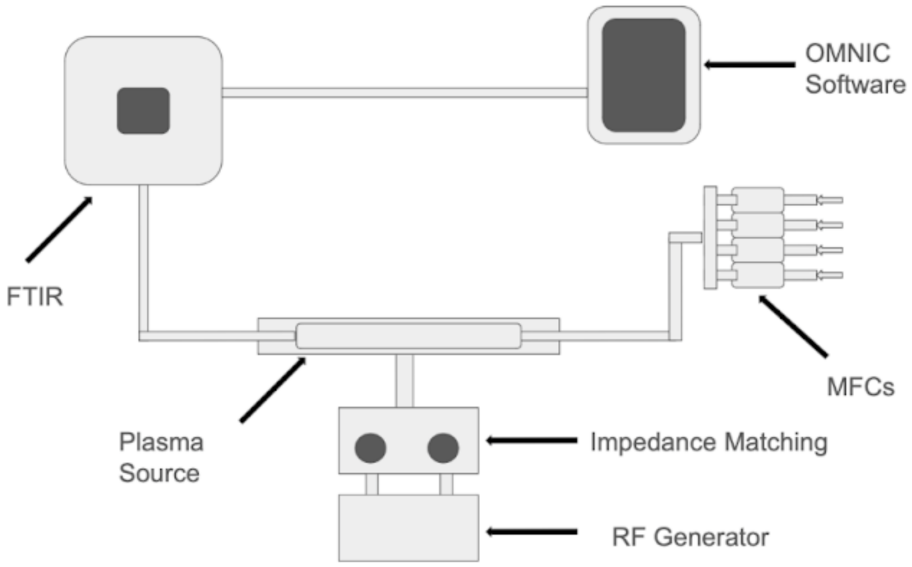

Figure 2.1: Diagram showing the apparatus arrangement used for conducting the project. Showing the power supply, inlet gas flow and the attached diagnostic equipment. Not shown is a water cooling system with a fan attached needed due to the heat build up of the plasma.

The set up is illustrated in figure 2.1, a capacitively coupled plasma system is employed. The set-up consists of two uncovered parallel plate electrodes (5 x 50 mm) separated by glass tubing enclosing the argon gas mixture (figure 2.2). It features a radio frequency (RF) power supply applied to one electrode, while the other is grounded. This configuration generates an electric field that accelerates the electrons in the mixture to produce and sustain the plasma. The system runs at room temperature and atmospheric pressure.

An impedance matching unit is connected between the RF generator and the powered electrode. This is to control the reflected power, reduce loss and ensure the RF power is efficiently coupled into the plasma.

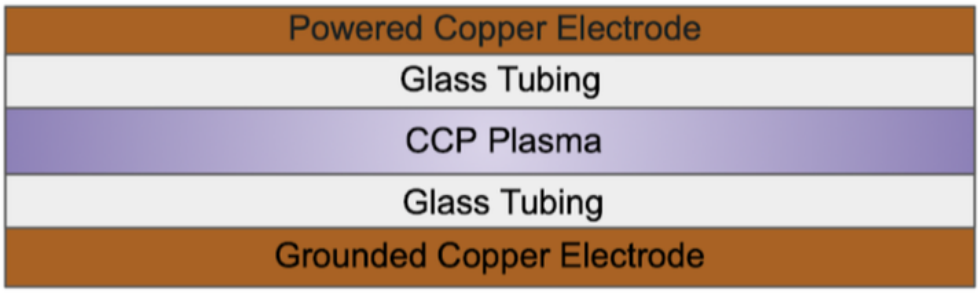

Figure 2.2: Diagram of the plasma set-up for a capacitively coupled RF plasma.

The plasma is generated within a borosilicate glass tube with a cross section of 4 mm x 0.5 mm and a wall thickness of 0.5 mm. A smaller interelectrode gap of 0.5 mm is used as it supports reliable operation in argon. Gas flow is controlled using mass flow controllers (MFCs). The flow rates used in the experiments are as follows:

- Argon (Ar): 250–2000 sccm
- Carbon Dioxide (CO_2): 0–35 sccm
- Nitrogen (N_2) and Oxygen (O_2): 0–25 sccm

Downstream of the discharge region, the glass tube is connected to a steel pipe that connects to the Fourier Transform Infrared Spectrometer (FTIR). The FTIR is used to produce the absorption spectrum of

the product. The piping length ($\approx$ 2.5 m) allows for products to have cooled before measurement. Measuring the products downstream allows for the reactions to continue taking place after the plasma, allowing for the measurement to contain stable products.

To ensure that each measurement reflects steady-state plasma conditions, between each measurement the plasma is given enough time to reach a point of equilibrium. To assess repeatability, 10 repeats were taken for each measurement for each experimental condition.

i. Fourier-Transform IR Spectrometer

A Fourier-Transform IR Spectrometer (Nicolet iS50, spectral resolution $1\,\mathrm{cm}^{-1}$, 10 m multi-pass cell) was used to carry out infrared (IR) absorption spectroscopy, to measure the absorption spectra downstream of the plasma source. To quantify results from the FTIR the absorbance is calculated through the integration of the peaks corresponding to isolated vibrational transitions of the target molecules.

Before every set of results recorded, a background FTIR measurement was taken. The background measurement was then subtracted from all the relevant spectra taken for that set of measurements to ensure baseline correction, therefore removing any unwanted signals from the FTIR machine and environment. Figure 2.3 demonstrates the necessity of the subtracted background to be able to analyse the spectra.

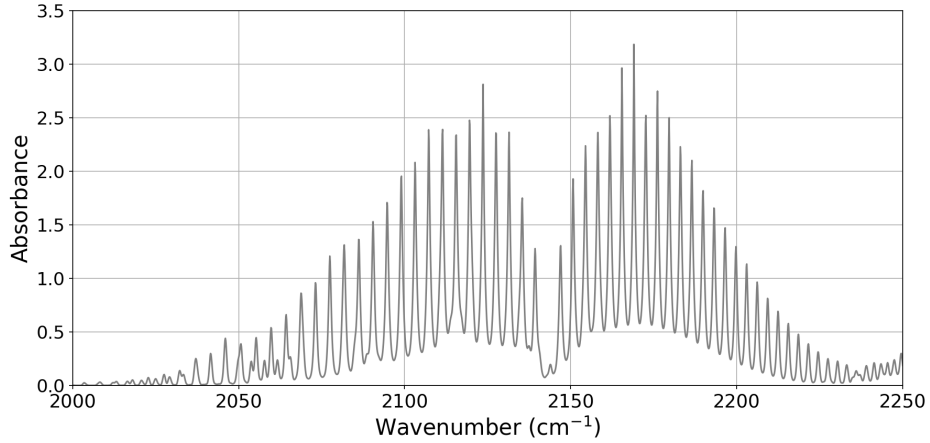

(a) CO peak FTIR spectrum with the background subtracted

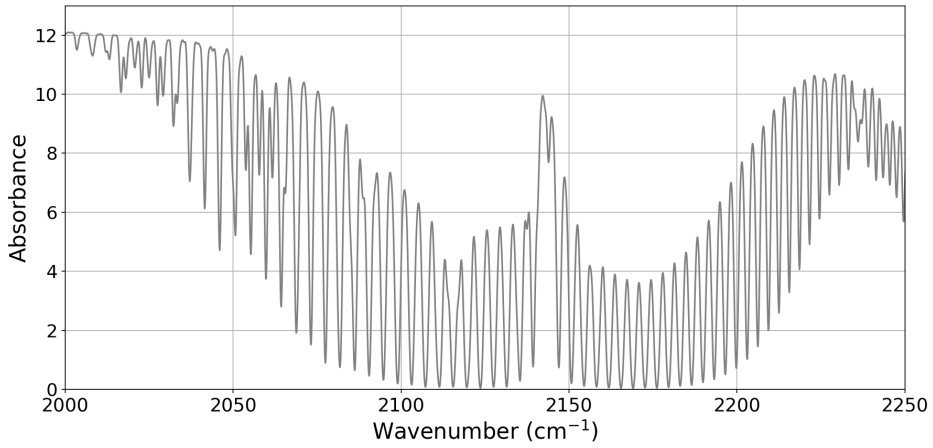

(b) Spectrum recorded with no background measurements taken into account.

Figure 2.3: Comparison of CO peak FTIR spectra measured consecutively under consistent conditions: (a) with background subtraction and (b) without background correction.

CO Absorbance

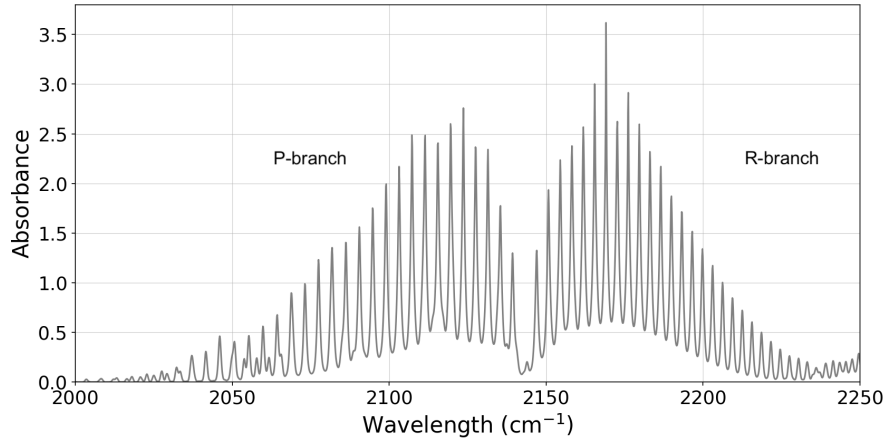

Figure 2.4: CO example of a FTIR absorbance spectrum, displaying P-Branch to the left and R-branch to the right. Operating conditions included 30 W generator power, 500 sccm total flow, 1.5% admixture CO_2.

Figure 2.4 displays an example FTIR absorption spectrum of carbon monoxide (CO) in the spectral range $2000 - 2250\,\mathrm{cm}^{-1}$, with the peak corresponding to transitions from the vibrational ground state to the first excited vibrational state. This peak arises from the C≡O stretching vibration, as CO is a diatomic molecule. A characteristic of the band is it exhibits 2 branches due to the rotational structure of the molecule, a P-branch and a R-branch. In IR spectroscopy, vibrational transitions are accompanied by rotational transitions because molecules rotate at room temperature. The rotational quantum number can change by ± 1 during absorption of a photon. Transitions with $\Delta J = +1$ form the R-branch, and those with $\Delta J = -1$ form the P-branch.

When integrating the CO peak the x and y limits on the FTIR graph have to be considered. The R-branch is excluded from the integration due to the tail of the branch overlapping with the nearby CO_2 band. Therefore, it is difficult to distinguish the contributions of the two compounds in that region.

Additionally, due to the FTIR having an optical path length of 10 m,

achieved through multiple internal reflections, the strongest absorption peaks can become optically thick, leading to deviations from the Beer-Lambert law. This means that it no longer follows the theoretically linear relationship between concentration and absorbance at high values. Therefore, to minimise the effect, regions with absorbance A>0.13 on the y-axis are excluded from the integration [44]. This is a choice taken in analysis to ensure that the trends are not representative of non-linear detector behaviour to avoid the possibility of underestimating or overestimating concentrations. Due to the y-axis limit all sets of CO spectra used consistent integration intervals, taken from the largest observed peak.

NO_x Absorbance

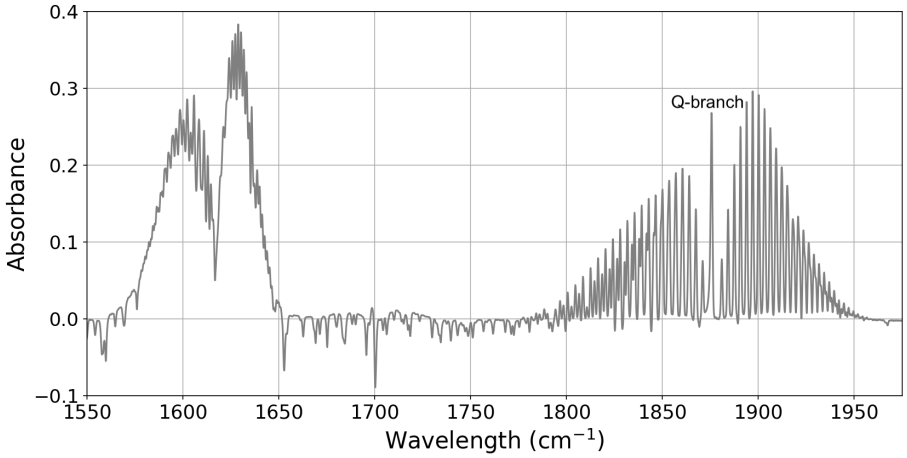

Figure 2.5: FTIR absorbance spectrum displaying NO and NO_2 absorption peaks. Displaying the Q-branch, the peak located between the R-branch and P-branch. Operating conditions consist of 30 W generator power, 1000 sccm total flow rate, 3% admixture and admixture ratio O_2:N_2 of 1:1.

Figure 2.5 displays a FTIR absorption spectrum for a plasma mixture containing NO_X, highlighting absorption features associated with NO and NO_2. To find the absorbance the whole peaks for both NO and NO_2 are integrated over $1775 - 1975\,\mathrm{cm}^{-1}$ and $1550 - 1650\,\mathrm{cm}^{-1}$ respectively. Although optical thickness is demonstrated later in this thesis, a

sufficiently detailed analysis was not undertaken to establish appropriate y-axis limits. Consequently, no y-axis limits have been applied.

The observed NO band corresponds to the region $1775 - 1975\,\mathrm{cm}^{-1}$, this peak is due to simple bond stretching, typical of diatomic molecules like NO. The peak is corresponding to the vibrational transition. A distinct characteristic of the band are its P- and R-branches, a Q-branch is also observed. The Q-branch arises because NO has an unpaired electron, which introduces electronic angular momentum and allows $\Delta J = 0$ transitions. Due to the difference in electronegativity between nitrogen and oxygen, NO possesses a permanent dipole moment, making these transitions infrared-active and therefore visible in the spectrum.

A strong band related to NO_2 is shown at $1550 - 1650\,\mathrm{cm}^{-1}$, this peak is attributed to asymmetric stretching vibration, one of the characteristic vibrational modes of this polyatomic molecule. The peak is corresponding to the vibrational transition. This band exhibits broad P- and R-branches because NO_2 is a bent, asymmetric top molecule with closely spaced rotational energy levels, resulting in overlapping rotational–vibrational transitions. The asymmetric stretch produces a large change in dipole moment, making the vibration highly IR-active and resulting in a strong absorption peak in the FTIR spectrum.

II. Calibration

i. *CO* Calibration

To convert the integrated areas of FTIR spectra into CO concentration for further analysis, a calibration procedure is performed. This calibration utilised data previously recorded by Steven Thomas, a former MSc student, obtained using the same experimental setup [45]. Initially, argon was introduced into the system in figure 2.1 with a flow rate of 1000 sccm to obtain the background readings and establish a baseline. Subsequently, CO was incrementally added to the gas mixture in steps of 1% (1-10%). The integrated area measurements are saved, which will later

be used to construct the calibration curve.

The calibration plot is generated with the integrated absorbance area on the y-axis and CO concentration on the x-axis. This relationship is fitted to a polynomial function constrained to pass through the origin (0,0), representing zero absorption when no CO is present. The generated calibration curve enables a conversion between experimental integrated absorbance areas and CO concentrations when CO_2 is used as the reactant gas. To obtain the CO concentration corresponding to the absorbance, the absorbance value is substituted as the x-value into the polynomial fit.

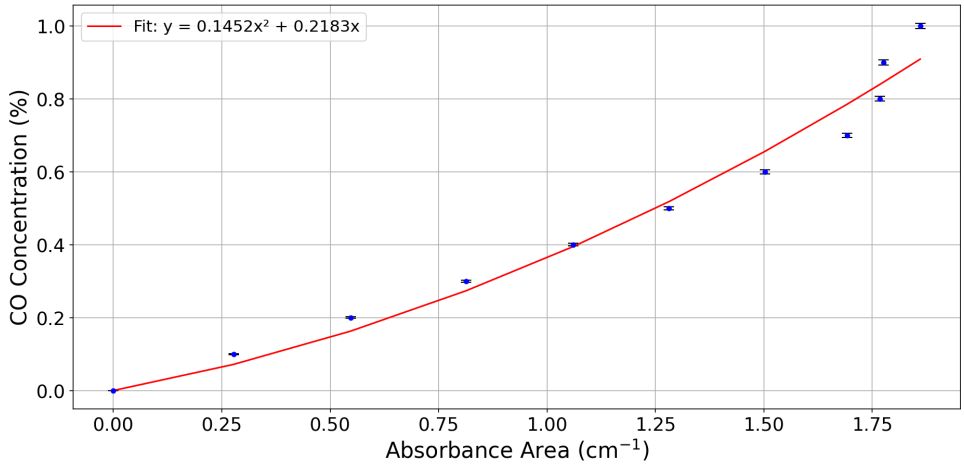

Figure 2.6: Calibration curve of known amount of CO admixture in the CO/Ar mixture against the corresponding integrated values under the absorption peak. Based on experimental data provided by Steven Thomas (former MSc student) [45]; analysis performed by the author. The operating conditions were 1000 sccm and 30 W of power.

A quadratic fit was applied to the data, yielding the expression :

$$f(x) = (0.1452 \pm 0.001372)x^2 + (0.2183 \pm 0.001934)x \qquad (2.1)$$

Although a quadratic function provided the best fit to the data, theoretically absorbance and concentration according to the Beer-Lambert law are a linear relationship. The non-linearity demonstrates an increasing deviation from the Beer-Lambert law at higher concentrations. This is

due to the law being only valid in optically thin conditions. Shown below figure 2.7 demonstrates the deviations from the calculated fit as the absorbance increases.

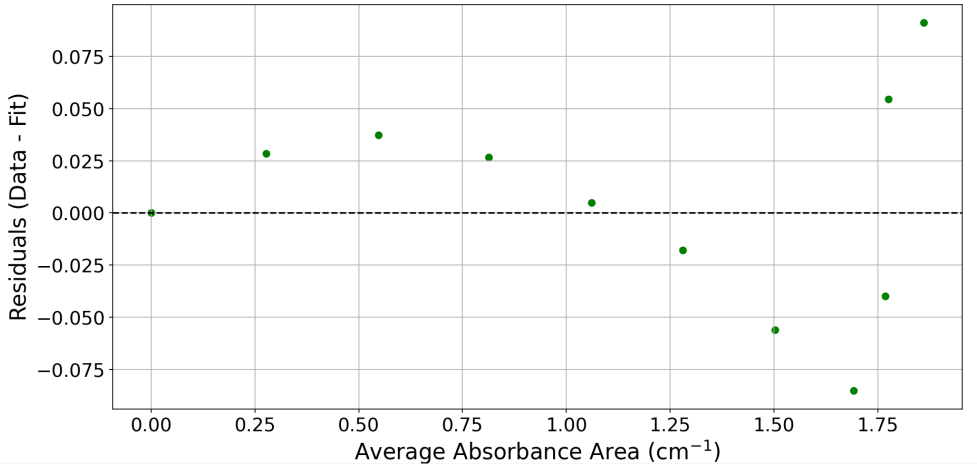

Figure 2.7: Displaying the residuals of the fit, differences between the collected plotted data and the fit attached to the plots.

ii. NO_x Calibration

To determine variables for comparison, calibration curves are used to convert the absorbance data from the FTIR into NO and NO_2 concentrations. The calibration curves were plotted through simulating multiple absorbance spectra at known concentrations. They are simulated using the HITRAN online database [46], inputting path length and spectral bands. To find the corresponding absorbance to concentration each spectra is integrated.

The integrated spectral range for NO was $1775 - 1975\,\mathrm{cm}^{-1}$, and for NO_2 the range $1550 - 1650\,\mathrm{cm}^{-1}$ was used. The fits plotted on both calibration curves is a polynomial fit due to deviations from linearity at higher concentrations. These non-linearities arise from a combination of increased optical thickness and saturation effects. As the simulation allows the optical path length to be specified, it is able to reproduce these effects that would also be observed experimentally. This behaviour is consistent with the Beer-Lambert relationship becoming non-linear at

higher concentrations. The calibration curves are applied using the same method as for CO_2, the experimentally determined integrated absorbance is substituted into the polynomial fit to determine the corresponding NO or NO_2 concentration.

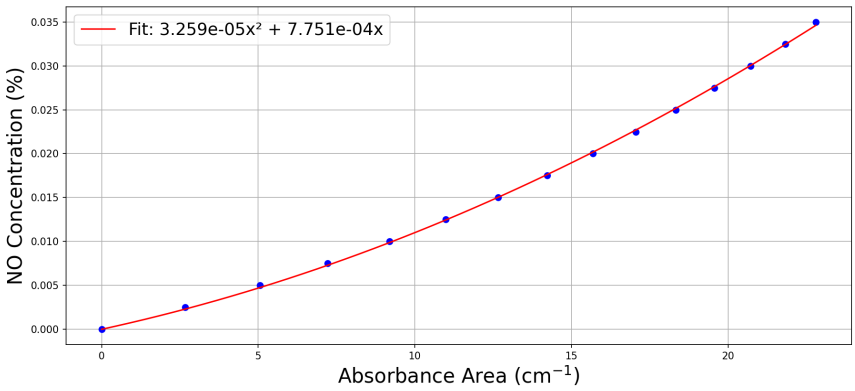

Figure 2.8: NO Calibration Curve, displaying the relationship between the integrated absorbance under the 1775-1975 cm^{-1} NO peak against the plasma's NO concentration.

The NO calibration curve in figure 2.8 produced the fit function :

$$f(x) = 3.259 \times 10^{-6}x^2 + 7.751 \times 10^{-4}x \tag{2.2}$$

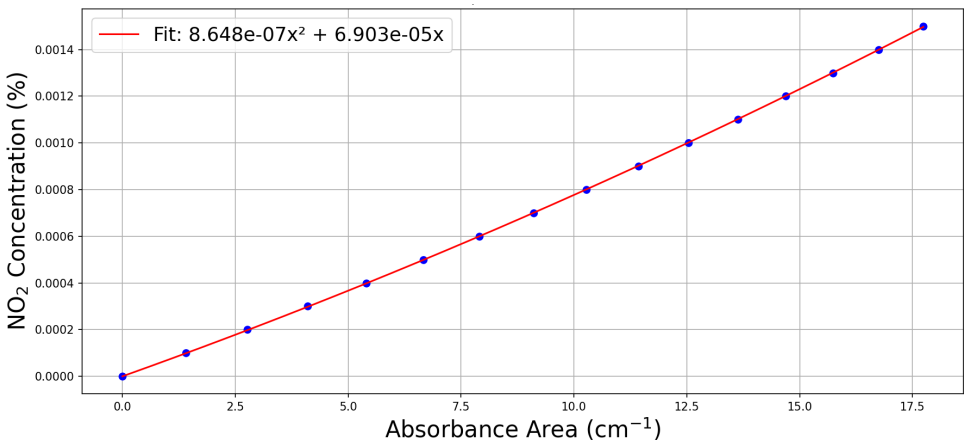

Figure 2.9: NO_2 Calibration Curve, displaying the relationship between integrated absorbance under the 1550-1650 cm^{-1} NO_2 peak and NO_2 concentration of the plasma.

The NO_2 calibration curve in figure 2.9 produced the fit function :

$$f(x) = 8.648 \times 10^{-7}x^2 + 6.903 \times 10^{-5}x \tag{2.3}$$

The HITRAN database includes the relevant CO transitions; however, it was not suitable for calibration in this work due to the discrepancies observed in previous experimental results. Although HITRAN provides theoretical spectroscopic parameters, earlier measurements obtained using similar experimental conditions account for instrumental and environmental effects. These experimental influences are not fully captured by standard HITRAN based models.

Errors are not produced for figures 2.8 and 2.9, due to the data being obtained from the HITRAN spectroscopic database. The associated uncertainties are negligible and do not produce significant errors. These errors would not be significant compared to the experimental errors.

III. Producing Comparable Variables

i. Variable Calculations

To be able to compare between parameter changes and to previous literature it is necessary to display the results with quantitative variables. The variables being calculated are product density, product yield, energy efficiency.

The product density is a direct measurement of the amount of product in the FTIR gas cell, expressed in molecules per cm^{-3}. This density is required to calculate other key variables. Similarly, the total flow, is needed for calculations which is the sum of the flow rates of the gases involved. These variables allow for the product yield to be determined, which is the proportion of the product formed against the amount of reactant introduced into the system, expressed as percentage. Product yield is important to show how effectively the reactants are converted to desired product.

Another metric produced is energy efficiency (μ), which quantifies the energy deposited into the plasma that contributes to the formation of the product, relative to the theoretical minimum energy required. This variable is a measure of evaluating practical viability. A preliminary step to calculating energy efficiency is determining specific energy input (SEI) which is the measurement of the energy supplied per reactant molecule flowing through the plasma. SEI is an effective way to normalise the energy efficiency across different conditions.

The product density is given by the following equation:

$$\text{Product density} = \text{Concentration} \times \text{Gas Cell Density} \tag{2.4}$$

The concentration is determined through figures 2.6, 2.8 and 2.9. The density of the gas cell can be calculated using a variant of the ideal gas equation that has standard temperature (T = 298 $\pm$ 3 K) and pressure (1 atm) values substituted. Therefore, the density of the gas cell is $(2.49 \pm 0.02) \times 10^{19}$ cm^{-3}.

Product yield is calculated through :

$$\text{Yield} = \left(\frac{\text{Product density}}{\text{Reactant admixture}} \right) \times 100 \tag{2.5}$$

Next, energy efficiency is calculated :

$$\mu = \frac{\Delta H}{S_{EI}} \times \text{yield} \tag{2.6}$$

To be able to calculate the energy efficiency the specific energy input (SEI) is required.

$$S_{EI} = \frac{\text{Generator Power}}{\text{number of molecules per second}} \tag{2.7}$$

$$S_{EI} = \frac{\text{Generator Power}}{\left(\frac{N_A}{V} \times \frac{T_F}{60} \times \frac{Reactant_{admixture}}{100}\right)} \tag{2.8}$$

$$V = \frac{RT}{P} \times 10^6 \tag{2.9}$$

$$V = \frac{8.3145 \times 298}{101325} \times 10^6 \tag{2.10}$$

$$V = 2.45 \pm 0.02 \times 10^4 \tag{2.11}$$

The total enthalpy values employed in the calculation of energy efficiency are given below:

$$\Delta H_{\mathrm{CO_2}} = 2.9 \text{ eV molecule}^{-1}$$

$$\Delta H_{\mathrm{NO}} = 0.935 \text{ eV molecule}^{-1}$$

$$\Delta H_{\mathrm{NO_2}} = 0.344 \text{ eV molecule}^{-1}$$

The dissociation of CO_2 has the dissociation enthalpy, $\Delta H = 2.9$ eV molecule^{-1}. In evaluating NO_X energy efficiency, the dissociation energies of N_2, $\Delta H = 9.756452$ eV molecule^{-1} [47], and O_2, $\Delta H = 5.116727$ eV molecule^{-1} [48], are considered, along with the energy released when the formation of compounds occur.

Furthermore, when comparing previous literature to current results, the conversion is equivalent to CO yield, as it is theoretically assumed that all converted CO_2 molecules form CO. However, in practice, the reactions can lead to the formation of by products such as carbon deposits. As a result, values reported in previous literature are often lower than the theoretical maximum.

Furthermore, energy efficiency and SEI values may be underestimated, as Equations 2.6 and 2.7 are based on the generator power displayed and do not account for the partitioning of energy between competing plasma processes. In particular, a fraction of the input power is dissipated

through electron-impact excitation and ionisation of both argon and CO species, alongside other collisional loss channels that do not contribute directly to net CO dissociation. These effects reduce the effective fraction of power available for conversion and may lead to an underestimation of the true process-specific efficiency. Nevertheless, SEI remains a widely adopted metric for comparative assessment in plasma conversion studies due to its simplicity and its suitability for benchmarking across different reactor configurations and operating conditions.

ii. Error Approximations

The errors associated with the temperature, power, flow rate and 10 repeats conducted on the same day are as follows. For the flow rate, the error associated with the controller is ±1% of the set value when the MFC operates in the top 80% of its range and ±0.2% of its maximum value when operating in the lowest 20%. The temperature is recorded as room temperature 298 K with an estimated error of 3 K. Errors for the repeats recorded on the day are calculated as the standard deviation. Finally, the uncertainty from the displayed generator power is 1% of the set point or 0.1% of the top value. Furthermore, power values correspond to the generator output power and therefore overestimate the power deposited into the plasma due to losses within the matching network and cables. While this does not affect the observed trends, absolute power values should be interpreted cautiously.

The uncertainties calculated for individual measurements account for contributions from temperature, power, flow rate, and the variability of ten repeat measurements performed on the same day. Within-day standard deviations for the density of the product were consistently below 1%, indicating that short-term variations in ambient conditions had a negligible effect on the results. In contrast, repeat measurements conducted on different days exhibited a standard deviation of approximately 5%, demonstrating that day-to-day variation was the dominant source of uncertainty. This increase in variability between days is possibly due to variations in ignition point, gas delivery, ambient conditions,

and electrode condition between experimental runs. Although temperature, power, and flow rate uncertainties were explicitly included in the individual measurement calculations, variations in these parameters also contribute to the observed day-to-day scatter. Consequently, the day-to-day standard deviation provides a measure of the overall reproducibility of the experimental system, encompassing both the quantified instrumental uncertainties and any additional uncontrolled variations between runs. As this contribution exceeded all other identified sources of uncertainty, a uniform uncertainty of $\pm 5\%$ was adopted for all density measurements and propagated to all quantities derived from them.

3

Results and Discussion

I. *CO* Results

i. Admixture Percentage

The first parameter investigated in relation to the measured CO concentration was the CO_2 admixture in the CO_2 and argon gas mixture. Throughout this series of measurements, the plasma operating conditions were held constant at a displayed generator power of 30 W and a total flow rate of 1000 sccm. The effects of CO_2 admixture on the produced CO density, CO yield, and energy efficiency are presented in figure 3.1(a)(b)(c).

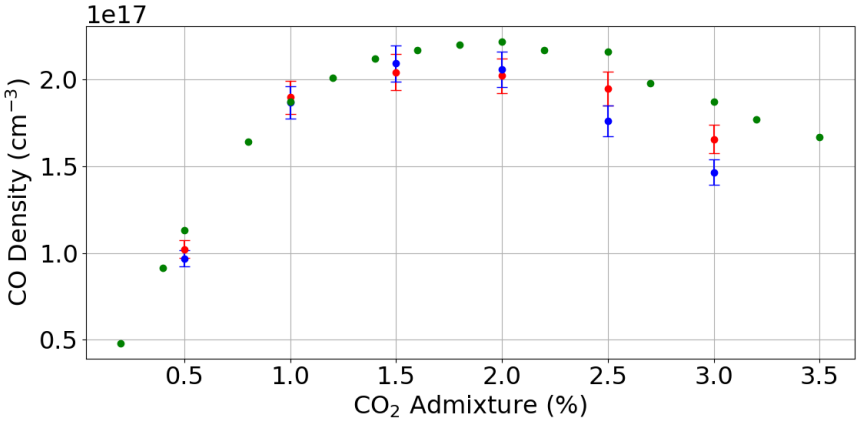

(a) CO Density [cm^{-3}]

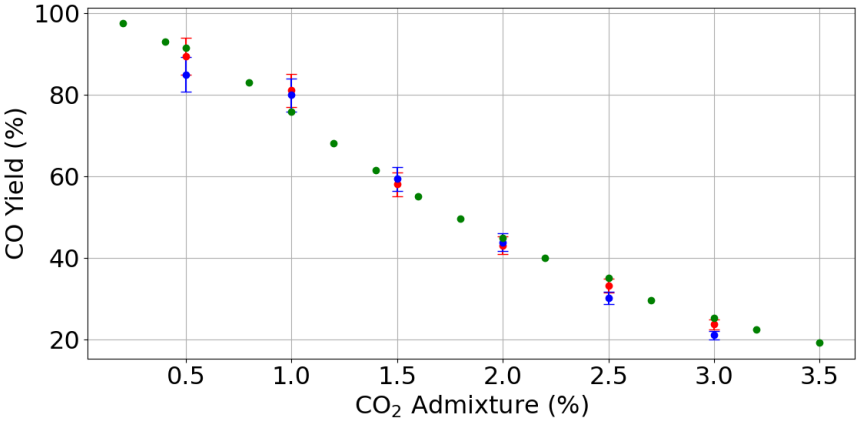

(b) CO Yield [%]

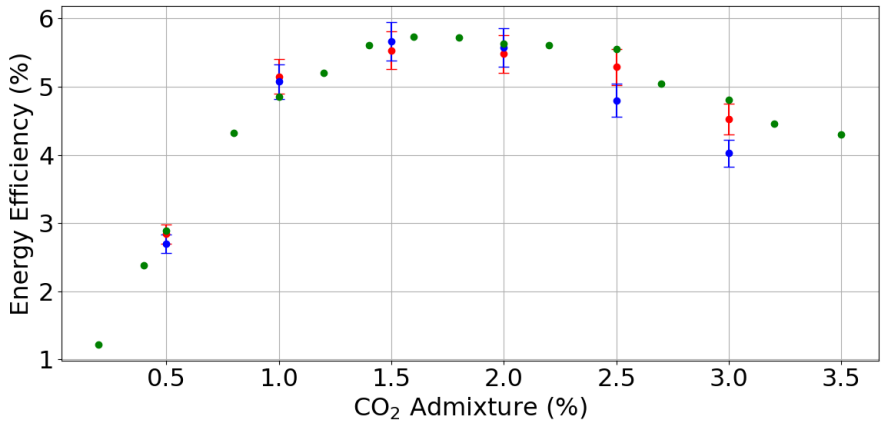

(c) Energy Efficiency [%]

Figure 3.1: All three variables plotted as a function of CO_2 admixture (%). The operating conditions were a constant flow rate of 1000 sccm and an power of 30 W. Red, blue, and green markers correspond to measurements from 15 January 2025, 24 February 2025, and the reference study [45], respectively.

Data collected during the project shows an alignment with previous literature, with a comparable set-up [45]. Between the previous literature [45] and the experimental results there is a small discrepancy at higher concentrations. Given the small day-to-day variability reflected in the experimental error, this difference is likely attributable to normal fluctuations rather than a systematic deviation. The consistency shown in the trends between the project data and literature enables confidence in the set-up, analysis methods and calibration models.

The peak CO density corresponds to an admixture of 1.5% with the maximum peaks for the data collected reaching $(2.091 \pm 0.105) \times 10^{17}\,\mathrm{cm}^{-3}$ and $(2.042 \pm 0.102) \times 10^{17}\,\mathrm{cm}^{-3}$. The initial increase occurring (before 1.5% CO_2 admixture) is due to an increase in CO_2 available for dissociation. As the CO_2 concentration increases past 1.5%, the CO density drops. As the admixture increases past 1.5% there is energy lost in CO_2 vibrational excitation, causing a reduction in the electron temperature,

therefore less ionisation, consequently lower electron density. In addition, in studies electron densities and electron mean energies calculated show that as admixture increases it results in lower direct electron impact dissociation [19].

Previous literature on noble gas plasma sources with trace molecular admixtures reports similar characteristics, with an early peak followed by a decrease or levelling off as the admixture increases. These observations have been reported for systems including He-N_2[49].

The CO yield in this project peaked at the lower admixtures, with the maximum peak recorded at a CO_2 admixture of 0.5%, on the 15/1/25 reaching 82.27±4.11% and on the 24/2/25, 77.87±3.89%. As the admixture increases beyond 0.5% the CO yield steadily decreases. The trend of lower admixture producing a larger CO yield is consistent with results produced previously [45]. Data from previous studies indicate the peak in CO yield occurs at an admixture of 0.2% with a 95% CO yield. Following the initial peak, as the admixture increases the CO yield decreases similar to the project's results.

The three sets of energy efficiency data exhibit consistent trends of demonstrating a peak between 1.5% and 2% admixtures, followed by a decrease as the admixture increases beyond 2%. This peak shaped behaviour is based on the same arguments as the peak in density. At higher admixtures the electron temperature drops, therefore a lower dissociation rate. As the power is approximately consistent throughout the experiment, the decrease in dissociation directly lowers the energy efficiency. The peak efficiency at 1.5 - 2% represents sufficient CO_2 availability and vibrational losses have not become significant.

In previous literature it shows that there can be a secondary rise in energy efficiency at a higher admixture if the plasma enters γ-mode, this is when there is an increase in secondary electron emissions which boosts the CO_2 conversion yield [50]. Figure 3.1(a) demonstrates the plasma remains in α-mode. The lack of a secondary maximum is possibly a result of

large admixture intervals. To examine if a second γ-mode–related peak occurs, smaller increments combined with qualitative analysis using time-resolved imaging as the modes have different characteristics, should be performed.

ii. Total Flow Rate

Next, the total flow rate was varied between 250 sccm to 2000 sccm, measuring CO concentration. The plasma operating conditions included a generator power of 30 W and a CO_2 admixture of 1.5%. The results shown in figure 3.2(a)(b)(c) demonstrate the effects of total flow rate on CO density, CO yield, and energy efficiency.

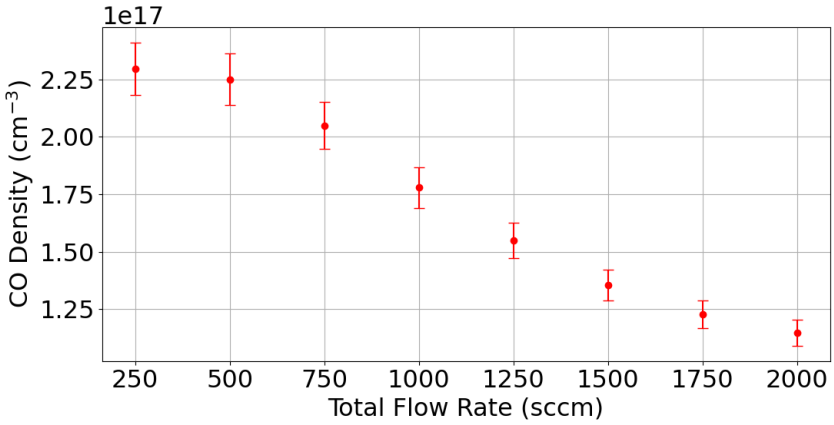

(a) CO Density [cm^{-3}]

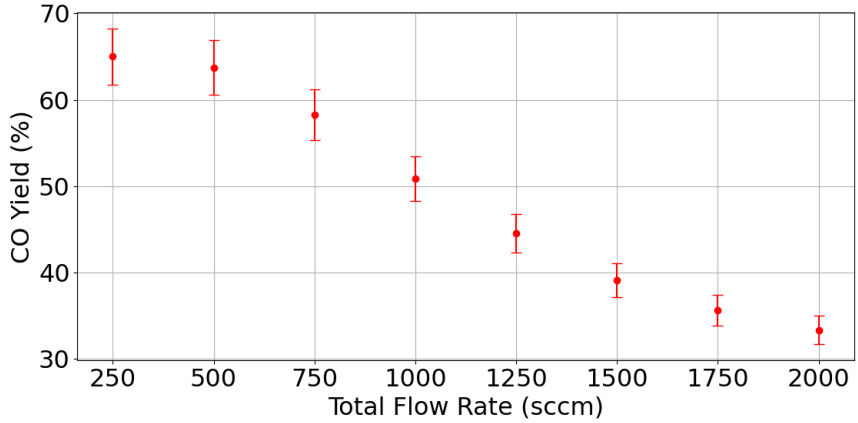

(b) CO Yield [%]

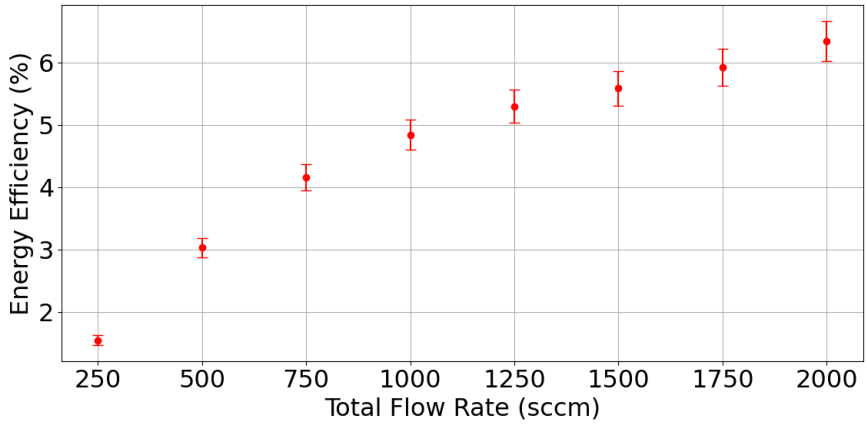

(c) Energy Efficiency [%]

Figure 3.2: All three variables are plotted as a function of the total flow rate of the mixture. The operating conditions consist of 1.5% CO_2 admixture and displayed generator power input of 30 W .

Both CO density and CO yield decrease monotonically with increasing flow rate in figure 3.2(a)(b). The similar trend is due to the dependence of CO yield on CO density and total flow rate. Figure 3.2(a) exhibits a maximum CO density of $(2.296 \pm 0.115) \times 10^{17}$ cm^{-3} at a 250 sccm flow rate. Similarly, the maximum for CO yield is shown at 250 sccm flow rate

reaching $61.48 \pm 3.07\%$ in figure 3.2(b). The decrease in both figures is a result of the increase in flow rate causing a reduction in residence time. A decrease in residence time reduces the time a particle spends within the system so there is consistent power but distributed between more particles as flow rate increases. Therefore, the viability of CO activation through collisions with electrons and excited species decreases, resulting in decreased CO conversion, also shown for dielectric barrier discharge [51].

The energy efficiency, however, increases with total flow rate, reaching $6.342 \pm 0.317\%$ at 2000 sccm. This improvement arises because, at lower flow rates, longer residence times results in the plasma acting as an energy sink, promoting non-productive processes such as gas heating and recombination. At higher flow rates, these losses are suppressed, and a greater fraction of the input power contributes to useful CO_2 dissociation, thereby improving energy efficiency. The increase in energy efficiency as flow rate increases has also been reported in literature for DBD reactors [52].

Furthermore, a trend displayed is the trade off between CO yield and energy efficiency as total flow rate increases, this inverse relationship has been widely reported in previous literature [53].

iii. Total Flow Rate and Admixture

Figure 3.3 shows admixture trends evaluated at 250, 500, 750, and 1000 sccm to assess their consistency across different total flow rates. The displayed generator power supplied remains constant at 30 W.

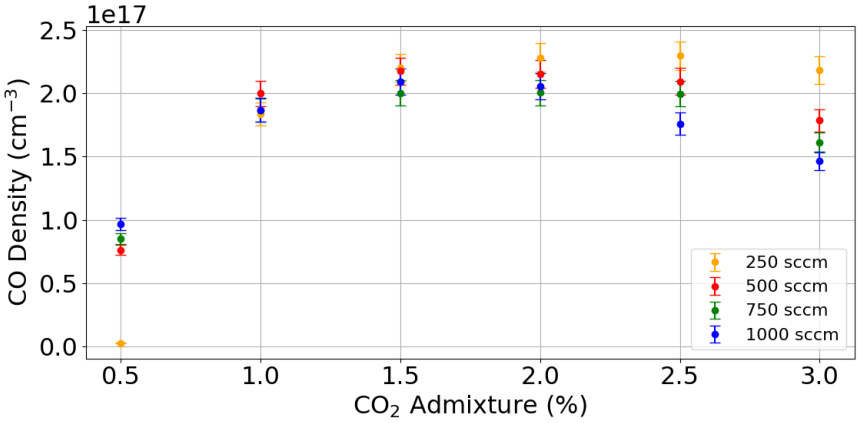

(a) CO Density [cm^{-3}]

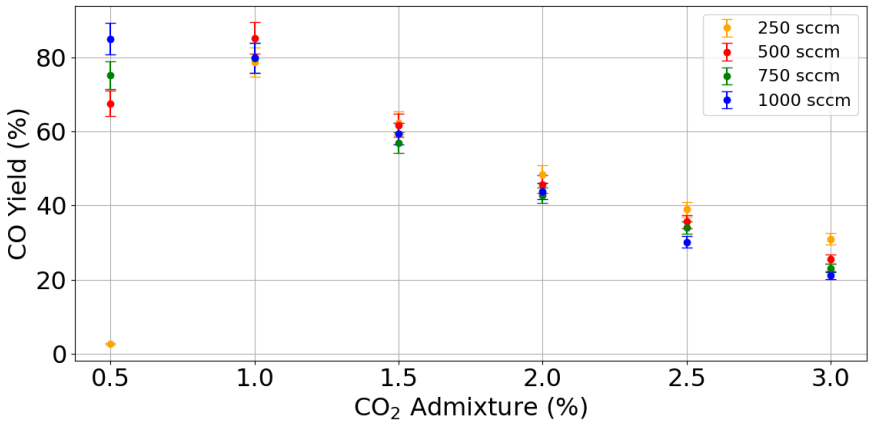

(b) CO Yield [%]

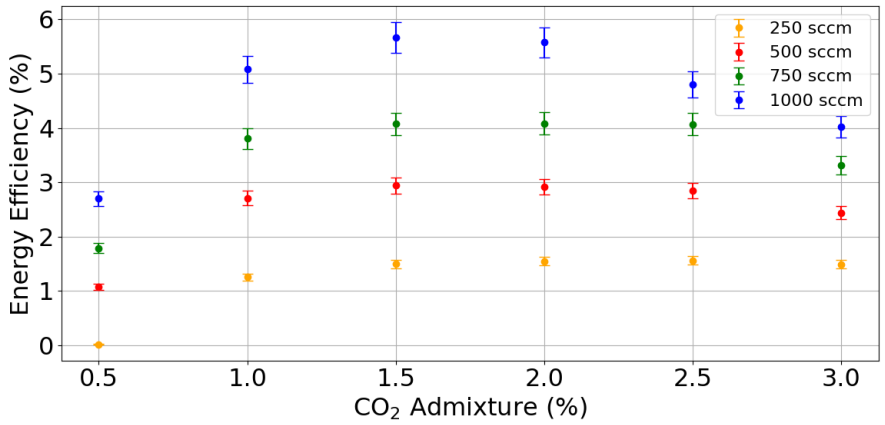

(c) Energy Efficiency [%]

Figure 3.3: Variables plotted against CO_2 admixture. The operating conditions included a constant displayed generator power input of 30 W. The curves represent results obtained at different total flow rates: 250 sccm (yellow), 500 sccm (red), 750 sccm (green), and 1000 sccm (blue).

An interest of the project is whether trends in plasma performance of varying CO_2 admixture persist when other control variables, such as total flow rate, are altered.

Figure 3.3(a) demonstrates that the general trend of a peak forming at intermediate CO_2 admixture is maintained across the several tested flow rates. The trends remain consistent, but the plotted points have variation on the y-axis. As the flow rate increases the peak of the curve is at lower admixtures. For CO density, the range of y-axis values widens as the admixture increases, at 1.5% admixture the range is calculated as 0.1104×10^{17} cm^{-3} and at 3%, 0.721×10^{17} cm^{-3}. Suggesting that variations in CO_2 admixture have less impact at lower total flow rates. Figure 3.3(a) demonstrates that lower flow rates (250 - 500 sccm) show a less pronounced peak. This effect is possibly due to a combination of an increased residence time at lower flow rates, which allows more reactions to occur as the admixture rises. It can also account for the inconsistencies in the trends at 0.5% and 1% admixture as the flow rates have reversed

effects with 1000 sccm producing the highest yield and density.

The data point corresponding to a CO concentration of 0.5% and a total flow rate of 250 sccm in Figures 3.3(a) and (b) deviates from the general trend observed in the dataset. This deviation is most likely attributable to the operational limits of the CO mass flow controller, which was required to operate at approximately 1.8% of its 70 sccm full-scale range. At such low fractions of the calibrated range, mass flow controllers can exhibit reduced accuracy and poor flow stability, resulting in unreliable delivery of the intended CO flow and increased measurement uncertainty [54]. Consequently, the effective CO feed to the plasma may be significantly lower than the set value, leading to reduced or negligible CO formation via CO dissociation. Therefore, figure 3.3(c) the data point at 0.5% and a total flow rate of 250 sccm should not be over interpreted that it is consistent with the trends.

Figure 3.3(b) displays, at total flow rates below 1000 sccm, a CO yield peak occurs at 1%, while at 1000 sccm, the peak appears at 0.5%, consistent with the results in Figure 3.2(b). The shift in peak position reflects changes in residence time and reactant renewal. Lower admixtures are better suited to higher flow rates, due to the reduced specific energy input resulting in lower electron temperature. Lower electron temperature favours vibrational excitation compared to direct electron excitation of CO_2. Enabling stepwise vibrational excitation increases production as it is the more common method for CO_2 dissociation. Following the peaks they all display the same trend for CO yield decreasing steadily as admixture increases, due to shorter residence times.

Energy efficiency demonstrates a consistent dependence on both total flow rate and admixture. Figure 3.3(c) indicates that increasing the total flow rate improves plasma energy efficiency, whereas variations in CO_2 admixture have a smaller, secondary effect. The highest energy efficiency is shown at 1000 sccm and the lowest corresponds to 250 sccm. With respect to CO_2 admixture, the energy efficiency remains relatively stable or slightly peaks across the studied range (0.5–3.0%). Similarly to the CO density, the spread of data points increases with the total flow rate.

At lower flow rates, energy efficiency remains nearly constant, suggesting that when gas flow is limited, the plasma's ability to transfer energy into dissociative processes becomes the rate-limiting step. This plateau likely arises because secondary recombination reactions and non-productive energy losses become dominant.

iv. Generator Power

The relationship between the generator power and the measured CO concentration is investigated. The generator power was varied between 15 to 30 W, as plasma ignition occurred after 10 W and the set-up was not safe to run at higher powers due to heat build up with the current equipment. The continuous variables of the system are a CO_2 admixture of 1.5% and a total flow rate of 1000 sccm. The results shown in figure 3.4(a)(b)(c) demonstrate the effects of the displayed generator power on CO density, CO yield, and energy efficiency.

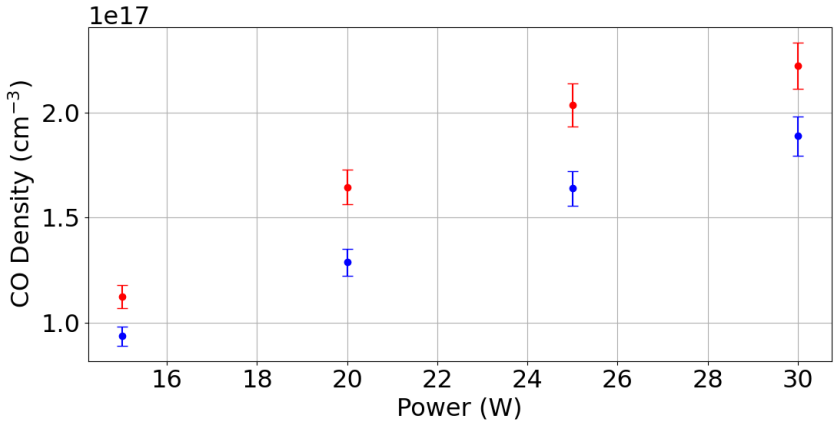

(a) CO Density [cm^{-3}]

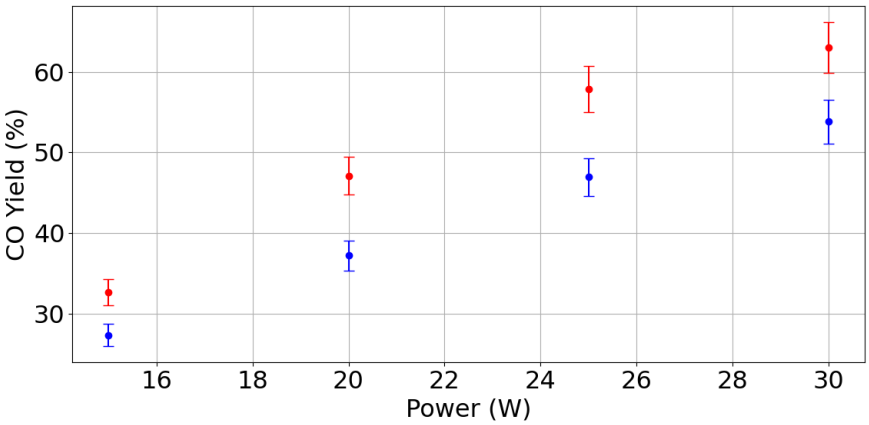

(b) CO Yield [%]

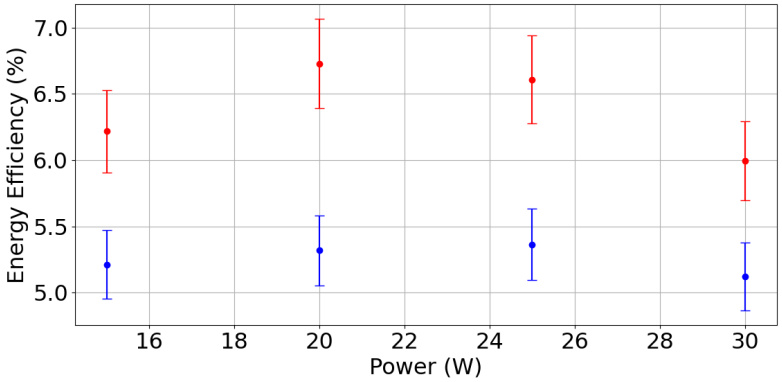

(c) Energy Efficiency [%]

Figure 3.4: Variables plotted against displayed generator power. The operating conditions were kept at a constant 1.5% CO_2 admixture and a total flow rate of 1000 sccm. Data collected on the 21 January 2025 appear in red, data from 10 March 2025 in blue.

Across both repeats, the point of ignition occurs between 10–15 W. Beyond this threshold, there is a steady increase in CO density and CO yield as the generator power increases. This is primarily due to an increase in ionisation rates, which generates a larger electron density. With more available electrons the rate of electron impact dissociation increases, leading to greater CO production.

In addition, as the generator power increases it strengthens the electric field, accelerating electrons and raising their temperature [55], [56]. Thereby altering the electron energy distribution function (EEDF). With the increase in electron temperature, the function broadens and the high energy tail becomes more pronounced, which corresponds to a growing population of electrons capable of effective dissociation. These observations are consistent with literature reports as the input power increases it enhances the production of high energy electrons and reactive species [57], thereby explaining the observed trends in CO density and CO yield. Similar trends have also been observed using microwave plasma sources [58].

Energy efficiency exhibits a modest peak at 20 W at $6.728 \pm 0.336\%$ on the 21st of January, on the 10th of March a maximum at 25 W with a value of $5.364 \pm 0.268\%$ is recorded. Beyond the optimal point, power is increasingly contributing to non-productive processes i.e gas heating, reducing the fraction of energy that is used for conversion. This can result in a decline or a plateau of the results at higher power levels. However, the data set is limited, when considering uncertainty the data plots remain level, demonstrating the primary use of power is for enhancing plasma stability.

The graphs are plotted using the power displayed by the generator, however a portion of this power is dissipated in the impedance matching network and power cables. Therefore, the power shown on the graphs is larger than the power deposited into the plasma. The trends and conclusions drawn remain valid, however the absolute power values should be interpreted with caution. To obtain more reliable power measurements, the actual value of power dissipated in the plasma can be calculated using the subtractive method [59], [60].

II. NO_x Results

i. Admixture Percentage

This section presents the influence of the total admixture percentage of O_2 and N_2 within the nitrogen–oxygen–argon gas mixture. Throughout this analysis, the O_2:N_2 ratio is maintained at 1:1, while the total flow rate and generator power are fixed at 1000 sccm and 30 W, respectively. Below in figure 3.5 the bar graphs display the density, yield and energy efficiency of NO (blue) and NO_2 (red), the same style of graphical representation is maintained throughout Figures 3.5 to 3.8.

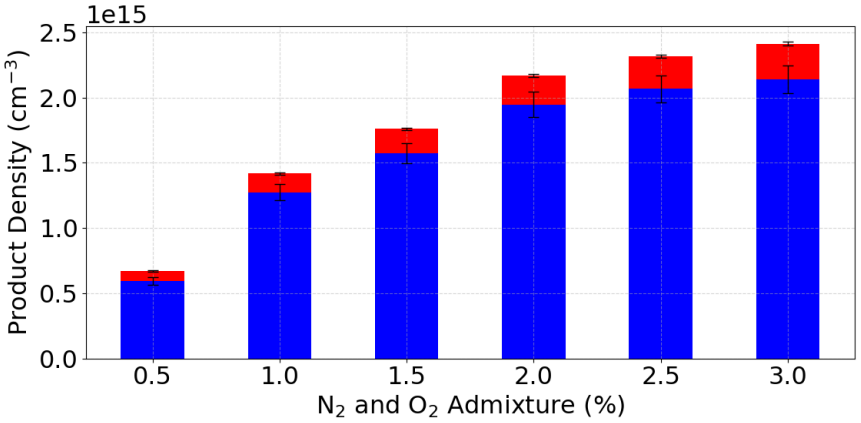

(a) NOx Density [cm^{-3}]

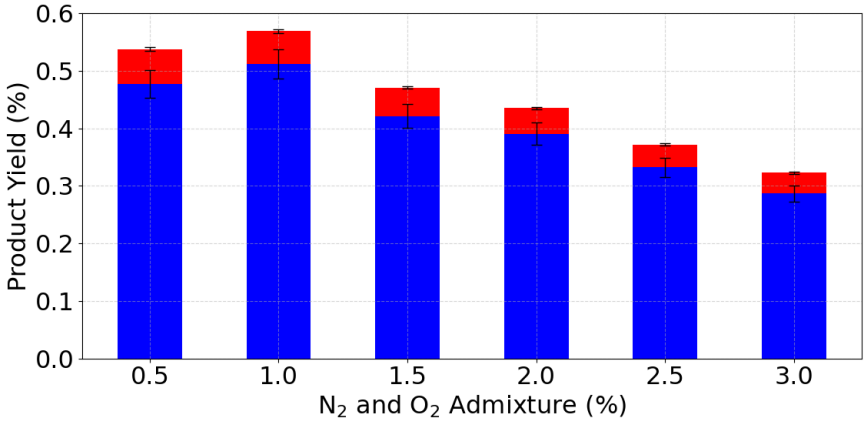

(b) NOx Yield [%]

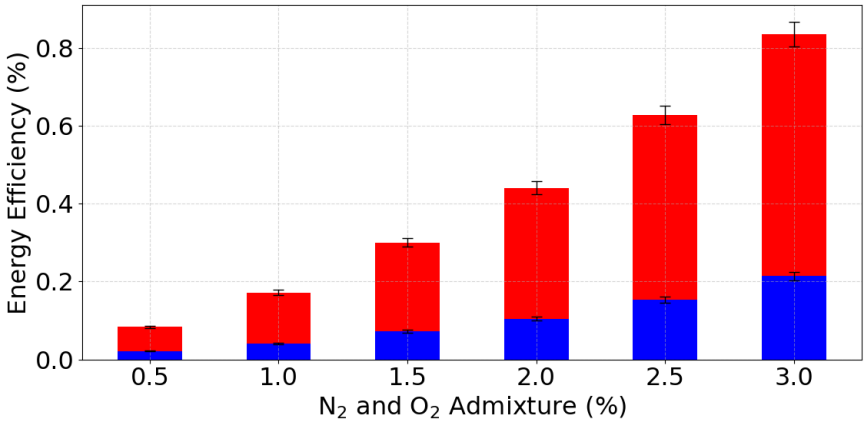

(c) Energy Efficiency [%]

Figure 3.5: Stacked bar plots illustrating the dependent variables against O_2/N_2 admixture. The operating conditions consist of 1000 sccm and 30 W generator power. The admixture includes an equal 1:1 (50% O_2 / 50% N_2) composition. Bar segments are colour-coded, with blue representing NO and red representing NO_2.

The NO and NO_2 densities measured using FTIR are shown in Figure 3.5(a). Increasing the admixture fraction increases the overall NO_X density of the product gas. A notable shift in the NO/NO_2 ratio is also observed with increasing admixture fraction, as the rate of increase in

NO_2 exceeds that of NO. Between admixture fractions of 1.5% and 2.5%, the NO density increases by 36.1%, whereas the NO_2 density increases by 46.3%. Figure 3.5(b) shows that the NO_X yield reaches a maximum at an admixture fraction of 1%, with a value of $0.5627 \pm 0.0285\%$, before gradually decreasing as the admixture fraction increases further.

The energy efficiency of NO_X production increases with increasing admixture fraction. The more rapid increase in the energy efficiency of NO_2 production is consistent with the previously observed changes in the rates of increase of the product densities. These results suggest that increasing the admixture fraction favours the oxidation pathway leading to NO_2 formation over the direct formation of NO.

ii. Total Flow Rate

Total flow rate was varied between 250 sccm and 1750 sccm, measuring NO and NO_X concentration. The operating conditions of the plasma included an admixture percentage 3%, the O_2:N_2 ratio is maintained at 1:1 and the displayed generator power 30 W. The range and conditions were chosen due to limitations on the MFCs. Results in fig 3.6 once again demonstrate density, yield and energy efficiency of NO and NO_2 production.

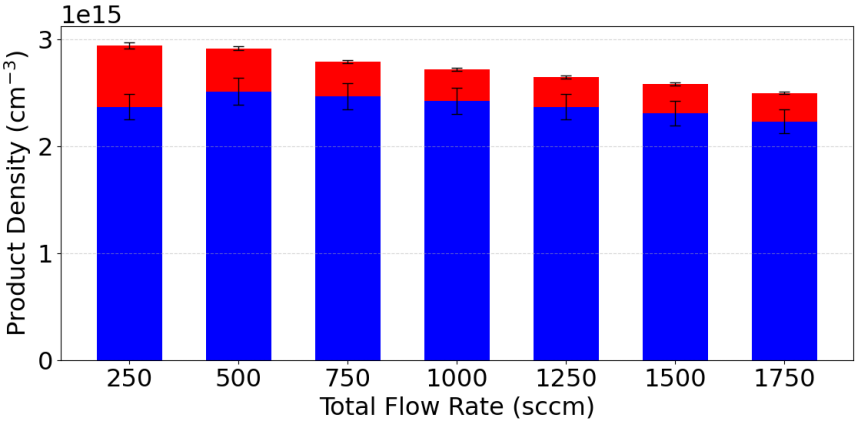

(a) NOx Density [cm^{-3}]

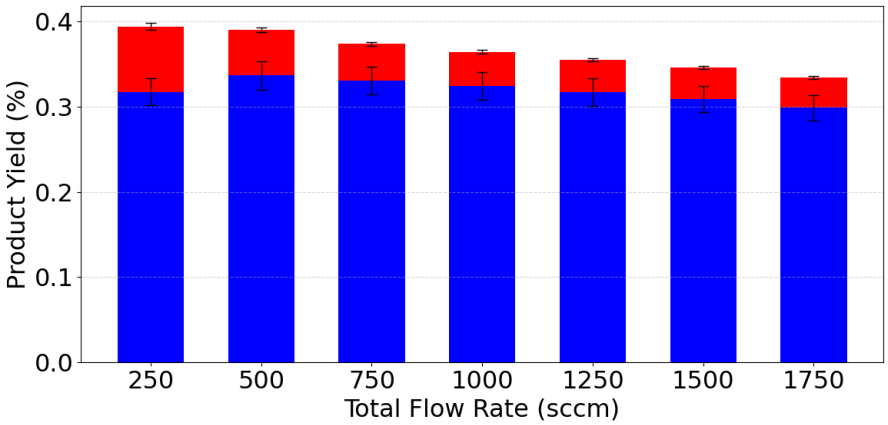

(b) NOx Yield [%]

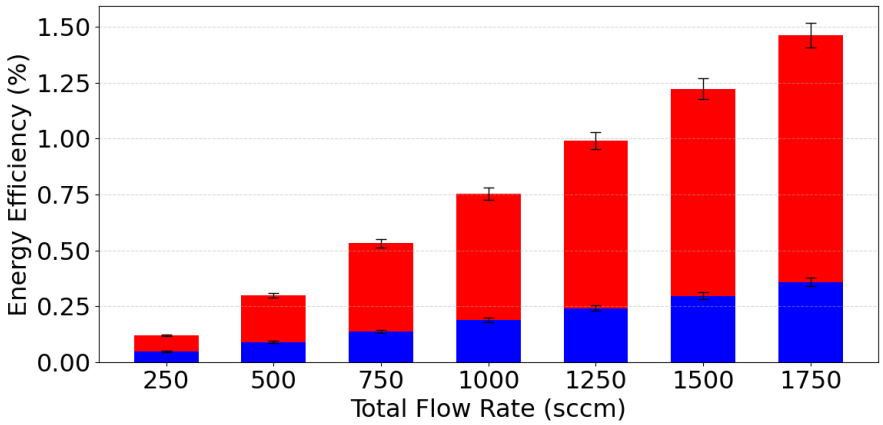

(c) Energy Efficiency [%]

Figure 3.6: Stacked bar plots illustrating the dependent variables against total flow rate of the gas mixture. The experimental conditions consisted of 30 W generator power, a 3% total admixture, and an equal 1:1 (50% O_2 / 50% N_2) composition. Bar segments are colour-coded, with blue representing NO and red representing NO_2.

The NO_X density and yield decrease progressively with increasing total flow rate, indicating a reduced conversion efficiency at higher throughputs. The maximum values for both parameters were found at 250 sccm recorded as $(2.9397 \pm 0.1470) \times 10^{15}$ cm^{-3} for product density and $0.39439 \pm 0.01972\%$ product yield. A minor deviation is observed at 500 sccm, where NO formation is enhanced relative to 250 sccm; however, this effect is counterbalanced by a corresponding decrease in NO_2, preserving the overall trend of a decreasing total of NO_X.

The general trend of the NO_X production decreasing is due to reduction in residence times. This is consistent with the behaviour observed and reasoning for production of CO with increasing total flow rate in figure 3.2. The ratio of products produced alters and decreases as the total flow rate increases. The production of NO_2 is more common at longer residence times as it allows for the further oxidation of NO to NO_2. Whereas at shorter residence times there is not sufficient time therefore

a larger proportion of the NO_X production is NO [37], [61].

The energy efficiency rapidly increases as the total flow rate increases due to the specific energy input increasing at a higher rate than the yield decreases. NO_2 is mainly responsible for this increase. NO_2 contributes most to this efficiency gain, as its formation from NO is exothermic and requires less additional energy than the dissociation of N_2 needed to form NO.

iii. O_2% of Admixture

The effect of varying the O_2:N_2 ratio was investigated using a series of compositions ranging from 2:10 to 10:2 in unit increments. Operating conditions of the plasma were held at total flow rate 1000 sccm, admixture 3% and generator power 30 W. With figure 3.7 displaying density, yield and energy efficiency of NO and NO_2 production.

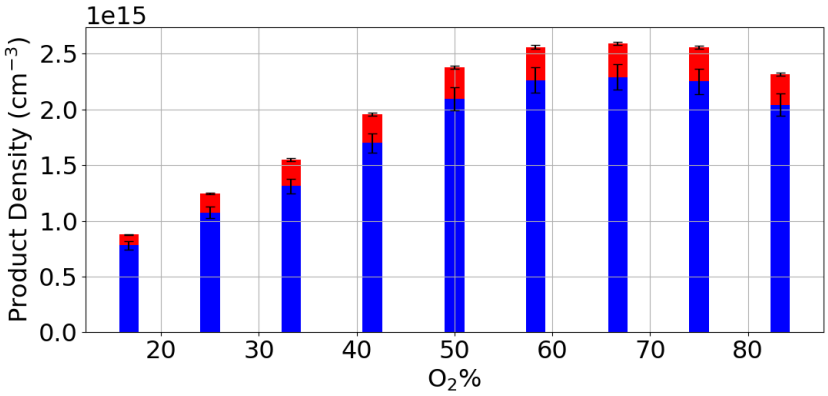

(a) NOx Density [cm^{-3}]

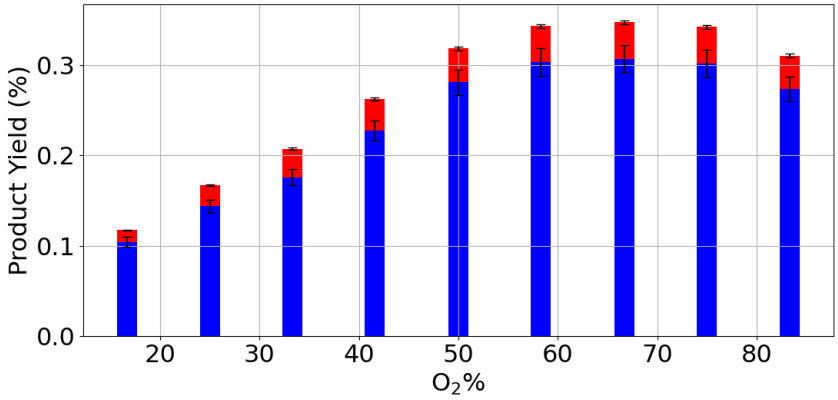

(b) NOx Yield [%]

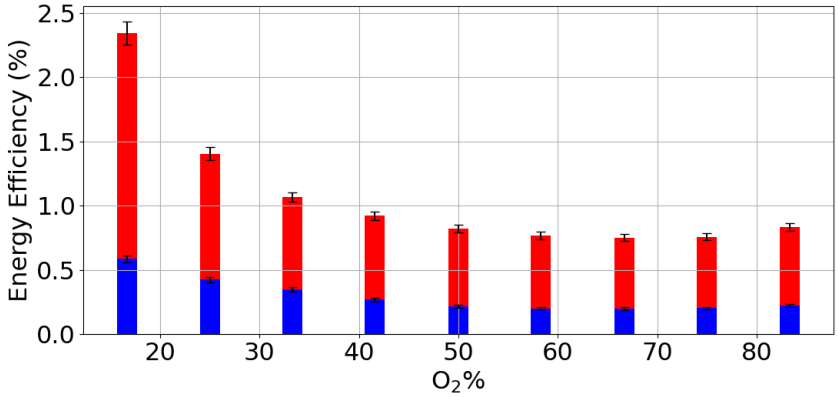

(c) Energy Efficiency [%]

Figure 3.7: Stacked bar plots illustrating the averaged dependent variables over two repeats against the O% in the O_2/N_2 admixture in argon. Experimental conditions include 30 W generator power, 3% total admixture and 1000 sccm flow rate. Bar segments are colour-coded, with blue representing NO and red representing NO_2.

The figure 3.7(a)(b)(c) displays the average density, yield and energy efficiency against the O_2% in the O_2/N_2 admixture. The figures show that the maximum density and yield of NO_X occurs at an O_2/N_2 ratio of approximately 2/1, indicating that this composition provides the most

favourable conditions for NO_X formation. The NO and NO_2 densities both increase as the percentage of O_2 increases up to around 66.6% O_2, after which they begin to decline, forming a bell-shaped curve. Previous studies using AC-driven dielectric barrier discharge have shown that nitrogen fixation reaches its maximum at O_2% levels of 60-70% [62]. At low percentages of O_2 there are insufficient levels of oxygen for oxidisation to form NO_X. As the O_2 fraction increases, electron-impact dissociation of O_2 becomes more frequent, generating reactive oxygen atoms that react with excited nitrogen species. At around 66.6% the system is optimised at a balance between enough oxygen for oxidisation and available N_2 for nitrogen source. Past this point the number of N_2 becomes a limiting factor as there is not enough for the abundance of oxygen. With an abundance of oxygen, radical recombination between the particles is likely. In addition, oxygen reacts with electrons differently to nitrogen, oxygen has a high electron attachment cross-section, which significantly reduces the population of free electrons responsible for molecular excitation and dissociation. At elevated oxygen concentrations, plasma electrons are increasingly captured by oxygen molecules through these attachment reactions.

The energy efficiency peaks at low O_2 concentrations and decreases continuously as O_2 increases until the minimum where it shows a slight increase after. This implies that although higher oxygen content promotes NO_X formation initially, the energy cost per NO_X molecule rises because of increasing energy losses to side reactions and combination steps.

An observation made during this set of experiments was as the oxygen percentage rose the plasma increased in length within the tube. At low oxygen percentages it was only glowing towards the exit of the glass tube and as the O_2 levels increased it lengthened to the full length of the electrode gap. This behaviour suggests a transition in discharge characteristics and plasma uniformity as a function of gas composition. At low concentrations of O_2, the discharge is confined to a smaller region near the outlet because plasmas with higher nitrogen content exhibit higher breakdown voltages. Localised channels of ionisation instead of a

uniform glow are a result from factors such as electrode geometry, the structure of the electric field, and gas flow.

As the oxygen levels increase, the visible expansion of the plasma can be attributed to oxygen's electronegativity, which enhances electron attachment, stabilising the discharge promoting a diffused glow. Furthermore, with increased O_2 percentage it reduces the gas conductivity, this spreads the voltage more evenly along the electrodes. In the future to connect these observations to quantitative results, optical emission spectroscopy could be utilised to measure emission from NO, NO_2, N_2^+, O, and O_2^+ at multiple positions. Which would create a link between plasma length and uniformity to NO_X formation [63].

iv. Generator Power

Lastly, the generator power on the production of NO and NO_2 was analysed. The operating conditions were optimised which was guided by the data presented in figures 3.5, 3.6, and 3.7, while also taking into account the limitations of the MFCs. Therefore, the ratio of O_2:N_2 was 2:1, 500 sccm flow rate and admixture composition of 3%. The graphs below demonstrate the density, yield and energy efficiency of the NO_X products produced.

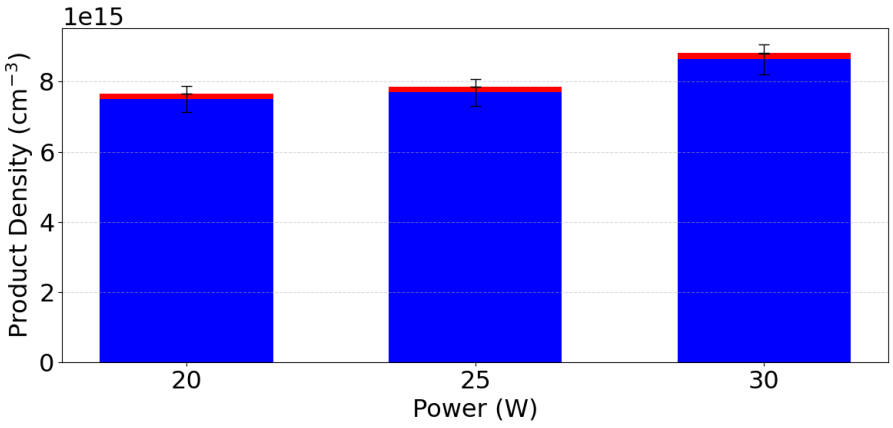

(a) NOx Density [cm^{-3}]

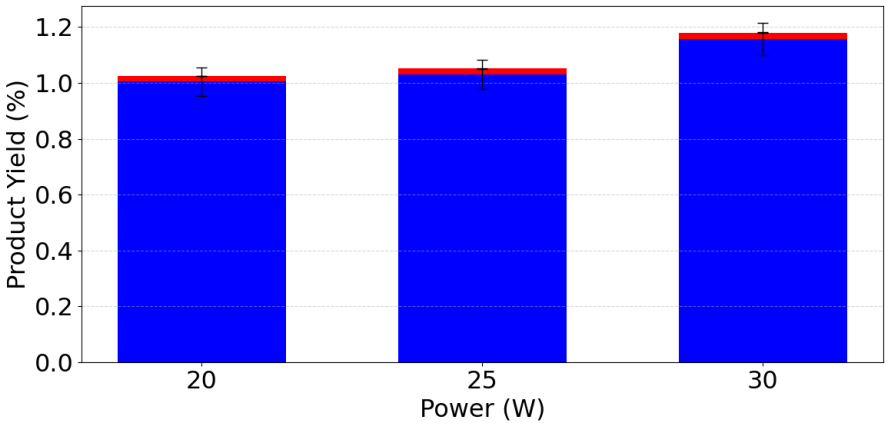

(b) NOx Yield [%]

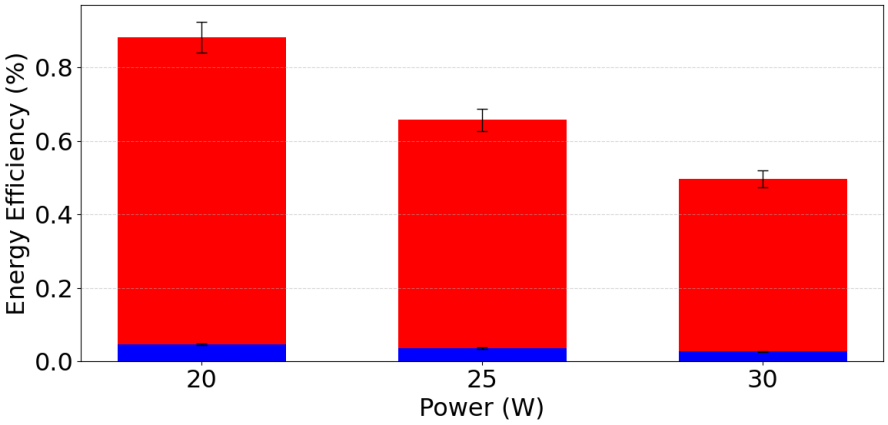

(c) Energy Efficiency [%]

Figure 3.8: Stacked bar plots showing the dependent variables as a function of displayed generator power. Experimental conditions consist of the total flow rate of 500 sccm, with a 8:4 ratio of O_2:N_2 with a 3% total admixture. Bar segments are colour-coded, with blue representing NO and red representing NO_2.

These results were obtained while operating under the optimised settings identified in previous experiments, demonstrating the potential for increased production when these factors are combined. The maximum product density and yield were recorded as $(8.8173 \pm 0.4409) \times 10^{15}$ cm^{-3}

and $1.180 \pm 0.059\%$ respectively. As the input power increases the NO_X product density increases. Input power and NO_X production are not linearly related because higher power leads to inefficient energy use, side reactions, and saturation of unproductive chemical pathways. Therefore, NO_2 yield increases more slowly than input power, and causing energy efficiency to drop at higher powers.

The results presented only range from 20–30 W, due to ignition only occurring after 15 W and operation above 30 W was not possible due to equipment safety constraints. The results produced before 20 W are negligible. To be more confident in the results an expanded power range would be efficient. Especially due to the yield increase between 25 to 30 W as it is 9.51% larger than the yield difference between 20 to 25 W. In addition, as discussed, the data uses generator power and not the power dissipated into the plasma. Therefore, applying the subtractive method to calculate the dissipated power, would be appropriate here [60].

4

Conclusion

This thesis investigated the optimisation of radio-frequency driven non-thermal plasma for CO_2 dissociation and NO_X formation as a preliminary step to ammonia production. With a focus on how the change in operational parameters affect product density, yield and energy efficiency. The bigger picture motivation of the project was considering how it fit into the decentralisation and sustainability of production.

The experiments conducted based on the dissociation of CO_2 demonstrated the optimal admixture was placed roughly at 1.5%. However, more significantly displayed the early admixture peak where there is a balance between available reactant molecules and electron energy. Total flow rate for CO_2 dissociation produced trends of a constant decrease in product density and yield due to a decrease in residence time as total flow rate increases. However, this is accompanied by increasing energy efficiency. Furthermore, figure 3.3 demonstrated the relaxation of trends of admixture as total flow rate increased and that the production has a larger dependence on flow rate. Lastly, for CO_2, generator power increase displayed an increase in dissociation rates with enhanced electron acceleration, with a decrease in energy efficiency as power increases past 20 W.

NO_X formation experiments displayed that a maximum NO_X density and yield occurred at around a 2/1 ratio of O_2/N_2, which is the balance

needed for oxidation and sufficient nitrogen. Increasing generator power had an increase in the product density and yield. Increasing the total flow rate demonstrated a decrease in both density and yield. Admixture affected the formation rate differently compared to CO_2 dissociation with a gradual increase as admixture increased. A further point of interest is the ratios of NO and NO_2 production were affected by the change in operating parameters and have a significant impact on the energy efficiency.

Overall, the work has shown a strong dependence on gas composition, flow rates and input power. Future work would first focus on expanding parameter ranges and decreasing the intervals between points to test the conclusions on scaled equipment to fully map trends. Next, to calculate the direct power dissipated into the plasma using the subtractive method. Finally, the project could also be expanded through exploring operating modes, plasma length and uniformity.

The findings and analysis discussed contribute to a comprehensive understanding of non-thermal plasma assisted chemical processes. With potential applications to support sustainable, small-scale production of CO and ammonia.

Bibliography

[1] Jürgen Meichsner, Martin Schmidt, Ralf Schneider, et al. *Nonthermal Plasma Chemistry and Physics*. Boca Raton, FL: CRC Press / Taylor & Francis, 2012, p. 564. ISBN: 9781420059168.

[2] A. von Keudell and V. Schulz-von der Gathen. "Foundations of low-temperature plasma physics—an introduction". In: *Plasma Sources Science and Technology* 26.11 (2017), p. 113001. DOI: 10.1088/1361-6595/aa8d4c.

[3] J. Chipman. "Free Energy of Water, Carbon Monoxide, Carbon Dioxide, and Methane: Their Metallurgical Significance". In: *Industrial & Engineering Chemistry* 24.9 (Sept. 1932), pp. 1013–1017. ISSN: 0019-7866. DOI: 10.1021/ie50273a013.

[4] R. Foresti, M. G. Bani-Hani, and R. Motterlini. "Use of carbon monoxide as a therapeutic agent: promises and challenges". In: *Intensive Care Medicine* 34.4 (2008), pp. 649–658. DOI: 10.1007/s00134-008-1011-1.

[5] "A Review of Non-Thermal Plasma Technology: A novel solution for CO_2 conversion and utilization". In: *Renewable and Sustainable Energy Reviews* 135 (2021), p. 109702. ISSN: 1364-0321. DOI: https://doi.org/10.1016/j.rser.2020.109702.

[6] J. Liu, L. Nie, and D. Liu. "Plasma for nitrogen fixation by using N2/O2 mixture: Reaction pathway, energy flow, and plasma reactor". In: *Plasma Processes and Polymers* 21.2 (2024), p. 2300153. DOI: https://doi.org/10.1002/ppap.202300153.

[7] D. Panchal, Q. Lu, K. Sakaushi, et al. "Advanced cold plasma-assisted technology for green and sustainable ammonia synthesis". In: *Chemical Engineering Journal* 498 (2024), p. 154920. ISSN: 1385-8947. DOI: https://doi.org/10.1016/j.cej.2024.154920.

[8] H. Chen, D. Yuan, A. Wu, et al. “Review of low-temperature plasma nitrogen fixation technology”. In: *Waste Disposal & Sustainable Energy* 3.3 (Sept. 2021), pp. 201–217. DOI: 10.1007/s42768-021-00074-z.

[9] C. A. Fernandez, O. Chapman, M. A. Brown, et al. “Achieving Decentralized, Electrified, and Decarbonized Ammonia Production”. In: *Environmental Science & Technology* 58.16 (2024), pp. 6964–6977. DOI: 10.1021/acs.est.3c10751.

[10] H. van ’t Noordende, G. Tubben, K. Rouwenhorst, et al. *Clean Ammonia Roadmap Report*. Tech. rep. Institute for Sustainable Process Technology (ISPT), Jan. 2024. URL: https://ispt.eu.

[11] M. F. H. Shikder, Y. Tang, E. Almehdawe, et al. “Risk incident analyses in the transportation of anhydrous ammonia as an emerging clean energy resource”. In: *Risk Analysis* 45.3 (2025), pp. 653–667. DOI: 10.1111/risa.17634.

[12] A. Rusin and K. Stolecka-Antczak. “Assessment of Syngas Storage Tank Hazards Taking Account of the Domino Effect”. In: *Energies* 17.8 (2024), p. 1857. DOI: 10.3390/en17081857.

[13] M. Y. Arshad, V. Hessel, A. Halog, et al. “Decentralisation transition in the chemical, energy, and waste management sectors: Innovations, opportunities, and sustainable pathways – A review”. In: *Sustainable Energy Technologies and Assessments* 76 (2025), p. 104307. ISSN: 2213-1388. DOI: https://doi.org/10.1016/j.seta.2025.104307.

[14] P. Chabert, T. V. Tsankov, and U. Czarnetzki. “Foundations of capacitive and inductive radio-frequency discharges”. In: *Plasma Sources Science and Technology* 30.2 (2021), p. 024001. DOI: 10.1088/1361-6595/abc814.

[15] F. Gorky, V. Storr, J. B. Jasinski, et al. “Cold-Plasma-Driven Ammonia Synthesis over Porous Silica: The Role of the Morphology”. In: *ACS Mater Au* 5.2 (Jan. 2025), pp. 385–396. DOI: 10.1021/acsmaterialsau.4c00159.

[16] Y. Xu, Y. Gao, L. Dou, et al. “Low-temperature plasma-enabled CO2 dissociation: a critical analysis of plasma setups and conver-

sion mechanisms toward scale-up valorization". In: *Green Chem.* 27.31 (2025), pp. 9332–9356. DOI: 10.1039/D5GC02037A.

[17] S. J. Hill, ed. *Inductively Coupled Plasma Spectrometry and its Applications*. Analytical Chemistry. Oxford, UK: Blackwell Publishing Ltd, 2007. ISBN: 978-1-4051-3594-8.

[18] J. E. Cooper. "Analysis of Nutraceuticals for Toxic Metals: Development and Validation of Sample Preparation Method". Master's Thesis. Clemson, SC, USA: Clemson University, May 2007.

[19] M. Ramakers, I. Michielsen, R. Aerts, et al. "Effect of Argon or Helium on the CO2 Conversion in a Dielectric Barrier Discharge". In: *Plasma Processes and Polymers* 12.8 (2015), pp. 755–763. DOI: https://doi.org/10.1002/ppap.201400213.

[20] S. Karimian, S. Payandeh, Z. Emam Bakhsh, et al. "Role of the atomic argon on the plasma characteristics of O2/N2 gas mixture". In: *Journal of Theoretical and Applied Physics* 19.2 (Apr. 2025), pp. 1–15. DOI: 10.57647/j.jtap.2025.1902.21.

[21] Robert J. Wandell, Huihui Wang, Radha K. M. Bulusu, et al. "Formation of Nitrogen Oxides by Nanosecond Pulsed Plasma Discharges in Gas-Liquid Reactors". In: *Plasma Chemistry and Plasma Processing* (2019). Version of Record available online. DOI: 10.1007/s11090-019-09981-w.

[22] H. Kildahl, L. Wang, L. Tong, et al. "Industrial carbon monoxide production by thermochemical CO2 splitting – A techno-economic assessment". In: *Journal of CO2 Utilization* 65 (2022), p. 102181. ISSN: 2212-9820. DOI: https://doi.org/10.1016/j.jcou.2022.102181.

[23] R. Z. Rios-Mercado and C. Borraz-Sanchez. "Optimization problems in natural gas transportation systems: A state-of-the-art review". In: *Applied Energy* 147 (2015), pp. 536–555. ISSN: 0306-2619. DOI: https://doi.org/10.1016/j.apenergy.2015.03.017.

[24] A. Bogaerts, T. Kozák, K. van Laer, et al. "Plasma-based conversion of CO2: current status and future challenges". In: *Faraday Discuss.* 183.0 (2015), pp. 217–232. DOI: 10.1039/C5FD00053J.

[25] R. Aerts, W. Somers, and A. Bogaerts. “Carbon dioxide splitting in a dielectric barrier discharge plasma: a combined experimental and computational study”. In: *ChemSusChem* 8.4 (2015), pp. 702–716. DOI: 10.1002/CSSC.201402818.

[26] J. Li, C. Ma, S. Zhu, et al. “A Review of Recent Advances of Dielectric Barrier Discharge Plasma in Catalysis”. In: *Nanomaterials* 9.10 (Oct. 2019), p. 1428. DOI: 10.3390/nano9101428.

[27] T. Nunnally, K. Gutsol, A. Rabinovich, et al. “Dissociation of CO2 in a low current gliding arc plasmatron”. In: *Journal of Physics D: Applied Physics* 44.27 (2011), p. 274009. DOI: 10.1088/0022-3727/44/27/274009.

[28] Huacheng Zhu, Yuqiang Huang, Shumeng Yin, et al. “Microwave plasma setups for CO2 conversion: A mini-review”. In: *Green Energy and Resources* 2.1 (2024), p. 100061. ISSN: 2949-7205. DOI: https://doi.org/10.1016/j.gerr.2024.100061.

[29] R. I. Azizov, A. K. Vakar, V. K. Zhivotov, et al. “Nonequilibrium plasmachemical process of CO2 decomposition in a supersonic microwave discharge”. In: *Akademiia Nauk SSSR, Doklady* 271 (July 1983). In Russian, pp. 94–98.

[30] I. Belov, V. Vermeiren, S. Paulussen, et al. “Carbon dioxide dissociation in a microwave plasma reactor operating in a wide pressure range and different gas inlet configurations”. In: *Journal of CO2 Utilization* 24 (2018), pp. 386–397. ISSN: 2212-9820. DOI: 10.1016/j.jcou.2017.12.009.

[31] T. Yong, H. Zhong, E. Pannier, et al. “High-pressure CO2 dissociation with nanosecond pulsed discharges”. In: *Plasma Sources Science and Technology* 32.11 (2023), p. 115012. DOI: 10.1088/1361-6595/ad066e.

[32] V. Ivanov, Ts. Paunska, S. Lazarova, et al. “Gliding arc/glow discharge for CO2 conversion: Comparing the performance of different discharge configurations”. In: *Journal of CO2 Utilization* 67 (2023), p. 102300. ISSN: 2212-9820. DOI: https://doi.org/10.1016/j.jcou.2022.102300.

[33] H. Liu. “Ammonia synthesis catalyst 100 years: Practice, enlightenment and challenge”. In: *Chinese Journal of Catalysis* 35.10 (2014), pp. 1619–1640. DOI: 10.1016/S1872-2067(14)60118-2.

[34] P. Berwal, S. Kumar, and B. Khandelwal. “A comprehensive review on synthesis, chemical kinetics, and practical application of ammonia as future fuel for combustion”. In: *Journal of the Energy Institute* 99 (2021), pp. 273–298. DOI: 10.1016/j.joei.2021.10.001.

[35] E. Meloni, L. Cafiero, M. Martino, et al. “Structured Catalysts for Non-Thermal Plasma-Assisted Ammonia Synthesis”. In: *Energies* 16.7 (2023), p. 3218. DOI: 10.3390/en16073218.

[36] E. Vervloessem, M. Aghaei, F. Jardali, et al. “Plasma-Based N2 Fixation into NOx: Insights from Modeling toward Optimum Yields and Energy Costs in a Gliding Arc Plasmatron”. In: *ACS Sustainable Chemistry & Engineering* 8.26 (July 2020), pp. 9711–9720. DOI: 10.1021/acssuschemeng.0c01815.

[37] B. S. Patil, N. Cherkasov, J. Lang, et al. “Low Temperature Plasma-Catalytic NOx Synthesis in a Packed DBD Reactor: Effect of Support Materials and Supported Active Metal Oxides”. In: *Applied Catalysis B: Environmental* 194 (2016), pp. 123–133. DOI: https://doi.org/10.1016/j.apcatb.2016.04.055.

[38] A. Bogaerts and G. Centi. “Plasma Technology for CO2 Conversion: A Personal Perspective on Prospects and Gaps”. In: *Frontiers in Energy Research* 8 (2020). ISSN: 2296-598X. DOI: 10.3389/fenrg.2020.00111.

[39] Y. Xu, Y. Gao, L. Dou, et al. “Low-temperature plasma-enabled CO2 dissociation: a critical analysis of plasma setups and conversion mechanisms toward scale-up valorization”. In: *Green Chemistry* 27 (Jan. 2025). DOI: 10.1039/D5GC02037A.

[40] A. S. Morillo-Candas, T. Silva, B. L. M. Klarenaar, et al. “Electron impact dissociation of CO2”. In: *Plasma Sources Science and Technology* 29.1 (2020), 01LT01. DOI: 10.1088/1361-6595/ab6075.

[41] D. Li, L. Zan, S. Chen, et al. “Direct conversion of N2 and O2: status, challenge and perspective”. In: *National Science Review* 9.12

(Dec. 2022), nwac042. DOI: https://doi.org/10.1093/nsr/nwac042. URL: https://doi.org/10.1093/nsr/nwac042.

[42] Z. Han, L. Song, P.-W. Shum, et al. "Generation and Applications of a Broad Atomic Oxygen Beam with a High Flux-Density via Collision-Induced Dissociation of O2". In: *Chinese Journal of Chemistry* 42.17 (2024), pp. 2010–2016. DOI: https://doi.org/10.1002/cjoc.202400081.

[43] T. Ayari, M. Desouter-Lecomte, R. Linguerri, et al. "State-to-state dissociative photoionization of molecular nitrogen: the full story". In: *Advances in Physics: X* 5.1 (2020), p. 1831955. DOI: 10.1080/23746149.2020.1831955.

[44] James Dedrick, Alex Foote, Andrew Gibson, et al. "Self-limiting trade-off between CO yield and CO_2 conversion energy efficiency in atmospheric pressure radio-frequency plasmas: picosecond laser spectroscopy". Manuscript in preparation.

[45] S. Thomas. "CO2 conversion to value-added chemicals using low temperature atmospheric pressure plasmas". PhD thesis. York, UK: University of York, Department of Physics, Aug. 2017.

[46] *HITRAN2020 Molecular Spectroscopic Database*. Available at https://hitran.org.

[47] P. Wang, S. Gong, Y. Li, et al. "Bond dissociation energy of N2 measured by state-to-state resolved threshold fragment yield spectra". In: *The Journal of Chemical Physics* 160 (2024), p. 014304. DOI: 10.1063/5.0187003.

[48] P. Wang, S. Gong, and Y. Mo. "Bond dissociation energy of O2 measured by fully state-to-state resolved threshold fragment yield spectra". In: *The Journal of Chemical Physics* 160 (2024), p. 164302. DOI: 10.1063/5.0207288.

[49] E. Wagenaars, T. Gans, D. O'Connell, et al. "Two-photon absorption laser-induced fluorescence measurements of atomic nitrogen in a radio-frequency atmospheric-pressure plasma jet". In: *Plasma Sources Science and Technology* 21.4 (July 2012), p. 042002. DOI: 10.1088/0963-0252/21/4/042002. URL: https://doi.org/10.1088/0963-0252/21/4/042002.

[50] Z. Ye, Q. Fu, L. Liu, et al. "CO2 conversion products in α and γ modes of radio frequency capacitively coupled plasma". In: *Journal of Applied Physics* (2025). DOI: 10.1063/5.0246946.

[51] Josep O. Pou, Eduard Estopañán, Javier Fernandez-Garcia, et al. "Sustainability Assessment of the Utilization of CO2 in a Dielectric Barrier Discharge Reactor Powered by Photovoltaic Energy". In: *Processes* 10.9 (2022). ISSN: 2227-9717. DOI: 10.3390/pr10091851.

[52] Nicola Lisi, Umberto Pasqual Laverdura, Rosa Chierchia, et al. "A water cooled, high power, dielectric barrier discharge reactor for CO2 plasma dissociation and valorization studies". In: *Scientific Reports* 13.1 (2023). DOI: 10.1038/s41598-023-33241-9.

[53] H. Hatami, M. Khani, S. A. Razavi Rad, et al. "CO2 conversion in a dielectric barrier discharge plasma by argon dilution over MgO/HKUST-1 catalyst using response surface methodology". In: *Heliyon* 10.4 (Feb. 2024), e26280. DOI: 10.1016/j.heliyon.2024.e26280.

[54] Kari Niemei. Private communication. Unpublished personal communication. 2026.

[55] H. Fatima, M. U. Ullah, S. Ahmad, et al. "Spectroscopic evaluation of vibrational temperature and electron density in reduced pressure radio frequency nitrogen plasma". In: *SN Applied Sciences* 3.6 (2021), p. 646. DOI: 10.1007/s42452-021-04651-z.

[56] P. J. Bruggeman and R. Brandenburg, eds. *Nonthermal Plasma Chemistry and Physics*. Taylor & Francis, 2013.

[57] Y. Yin, T. Yang, Z. Li, et al. "CO_2 conversion by plasma: how to get efficient CO_2 conversion and high energy efficiency". In: *Physical Chemistry Chemical Physics* 23 (2021), pp. 7974–7987. DOI: 10.1039/D0CP05275B.

[58] M. Bresser, K. Wiegers, A. Schulz, et al. "CO Generation from CO_2 Using an Atmospheric Microwave Plasma Process". In: *Chemie Ingenieur Technik* 97.5 (2025), pp. 479–486. DOI: 10.1002/cite.202400157.

[59] J. Golda, J. Held, B. Redeker, et al. "Concepts and characteristics of the 'COST Reference Microplasma Jet'". In: *Journal of Physics*

D: Applied Physics 49.8 (Jan. 2016), p. 084003. DOI: 10.1088/0022-3727/49/8/084003.

[60] Andrew Thomas West. "Optical and Electrical Diagnosis of Atmospheric Pressure Plasma Jets". Doctor of Philosophy. University of York, Apr. 2016.

[61] Xiaolong Hao, Amber M. Mattson, Chelsea M. Edelblute, et al. "Nitric Oxide Generation with an Air Operated Non-Thermal Plasma Jet and Associated Microbial Inactivation Mechanisms". In: *Plasma Processes and Polymers* 11.11 (2014), pp. 1044–1056. DOI: 10.1002/ppap.201300187.

[62] Pradeep Lamichhane, Nima Pourali, Evgeny V. Rebrov, et al. "Energy Intensified Nitrogen Fixation Through Fast Modulated Gas Discharge from Pyramid-shaped Micro-electrode". In: *Plasma Chemistry and Plasma Processing* 44.3 (2024), pp. 1369–1392. DOI: 10.1007/s11090-023-10376-1.

[63] Fermín Castillo, H. Martínez, O. Flores, et al. "Optical emission spectroscopy and modeling of DC CO_2–N_2–He mixture plasma". In: *Revista Mexicana de Física* 71.3 May-Jun (May 2025). DOI: 10.31349/RevMexFis.71.031501.